Ad-hoc modeling of closed-cell foam microstructures for structure-properties relationships

M. Dabo, T. Roland, G. Dalongeville, C. Gauthier, P. Kekicheff

Ad-hoc modeling of closed-cell foam microstructures for structure-properties relationships

M. Dabo[1], T. Roland[✉, 1, 2], G. Dalongeville[1], C. Gauthier[1], P. Kékicheff[1]

[1] *Institut Charles Sadron (ICS), UPR22 C.N.R.S, Université de Strasbourg, 23 rue du Læss, 67034 Strasbourg, France*
[2] *INSA de Strasbourg, 24 Boulevard de la victoire, 67000 Strasbourg, France*

✉ Corresponding author: thierry.roland@ics-cnrs.unistra.fr

Abstract

During the formation of open-cell foams the relevant driving force besides gas pressure comes from surface tension which controls area minimization of the topology. Accordingly, the Surface Evolver software expressly developed to shape liquid surface by minimizing their energy given various constraints such as bubble volumes allows computing very realistic models of equilibrium foam microstructures. However, when considering non-equilibrium foam (dense foam) or the formation of closed-cell foams where films between adjacent cells are thick, a more complete model would have to consider the expansion process as a whole and include the viscous flow of the suspending fluid, which eventually solidifies to form the solid phase of the foam. This situation has not been investigated computationally because the problem size is too large and despite several attempts there remain significant challenges to integrate the foaming process knowledge into mathematical formulas. In a continuing effort to establish structure-properties relationships, an ad-hoc model is detailed to generate numerical closed-cell foam microstructures that resemble the real ones for a medium to a high porosity range. Inspired from a physical description of the manufacturing process making use of chemical blowing agent, a dynamic approach taking into account the influence of the temperature on the physical material characteristics is proposed. It allows the nucleation of cells, their growth through gas expansion, and the interactions between growing cells to be taken into account simultaneously. The large variety of generated microstructures with porosities spanning the few to 95 percents range is compared to real polymeric closed-cell foams whose microstructures were determined by X-ray microtomography at high spatial resolution. These structures are then used as templates to generate realistic finite element models and study the mechanical properties.

***Key words**: polymeric solid foam, mechanical properties, modeling, numerical foam microstructure, X-ray tomography analysis.*

I. INTRODUCTION

Polymeric solid foams combine attractive mechanical, thermal, chemical and diffusive transport properties which are interesting for light-weight structural problems. However, in order to diversify their applications in engineering systems and to make them even more efficient in the fields of health, transportation, construction, soundproofing and energy absorbing materials, it is important to fully understand the influence of the cellular microstructure on the effective macroscopic properties of the polymeric foam material. The task is not easy as the properties encountered at a macroscopic scale result from the combined interaction between the microstructure foam morphology and the physicochemical characteristics of the material constituting the cell walls. The latter is a complex mixture of different chemicals in proportions and distributions specific to the polymer foaming process and related to their ultimate tiny spatial scale. It is therefore often not possible to obtain or to mimic such materials of ill-defined nature when sufficiently large volumes and masses are required for experimental determinations of their bulk properties (such as their mechanical behavior: compression, traction, etc.). In addition to this limitation, the complexity of microstructures and foam morphology makes any genuine and systematic investigation of the effective macroscopic properties of real polymeric foams experimentally challenging. One way of overcoming this difficulty is to turn to numerical simulations. Thus, it is possible to develop an understanding of the correspondence between the characteristics of the microstructure and the effective macroscopic foam response.

However, it is generally recognized that generating polymer foam microstructures is a computational challenge since realistic foam microstructures are complex. Several structural models have been created by replacing the real foam microstructures with those having simpler geometries. The models can be classified into two categories: those with regular and irregular structures. Regular structure models are often obtained by paving simple elementary cells in 2D (square, circle, triangle…) or in 3D (cube, sphere, tetrahedron...). W. Thomson (Lord Kelvin) proposed in 1887 a tetradecahedron as the best elementary model for packing equal-sized objects together to fill space with a minimal surface area [1]. This structure, relevant in liquid foams (Plateau's laws) has been widely adopted for modeling polymeric foam structures. Kraynik and Warren have for example used it to perform a micromechanical analysis of the linear elastic behavior of low density open cell foams [2]. A major drawback of the models based on regular structures is that only the relative density of the foam (i.e. porosity) is taken into account. As a consequence, these models are not capable of describing the variation in the distributions of cell sizes, or shape, or positions of the cells for structures

having the same porosity, and hence not capable of describing the full macroscopic mechanical behavior of the foam satisfactorily. This is why other models based on more realistic geometrical descriptions have been proposed, such as those based on irregular structures. Voronoi tessellation of the space is often used for random cell structure generation. The process for generating these tessellations resembles the process of liquid foam formation where bubbles grow at a uniform rate. Whenever the bubbles touch each other, growth stops at the contact point but continues elsewhere. Due to this similarity between the mathematical procedure of the Voronoi tessellation and the physics of foam production, the tessellations can be created such that the cell geometry complies with Matzke's experimental work [3] on the liquid bubbles shapes. Roberts and Garboczi [4] created 3D Voronoi models of open and closed cell foams. Valuyskikh [5] was able to extract irregular stochastic models by deflecting cell centers with a regular structure of tetradecahedrons. We note however that by generating a random structure from an initial regular structure without any constraint on the cell morphology, the structure obtained will lack important characteristics of the real foam geometry. To overcome this problem, the tessellation is usually relaxed by minimizing the total surface energy area while preserving the cell-volume distributions using the Surface Evolver software. This relaxation process creates several topological transitions within the local cell neighborhood that leads to soap froth that fully respects Plateau's laws. In particular, compared with the Voronoi tessellation, slightly curved faces and edges and significantly fewer short edges have been observed [6]. In this regard, the Surface Evolver software originally developed by K. Brakke [7] to study a liquid surface shaped by surface tension and subject to various constraints, has allowed to make a significant leap forwards in the modeling of equilibrium foam microstructures. This approach is particularly interesting when large porosities are considered; however by nature it becomes inappropriate for non-equilibrium foam microstructures, where a coupling between surface tension and viscous stresses has to be considered. For such non-equilibrium foam microstructures, the mathematical algorithm for surface area minimization can no longer give a relevant description of the morphology. In addition, certain physical "ingredients" should be involved.

Two industrial foam structures of medium porosity are illustrated in Fig.1. For these foams, it is difficult to fit the cell shape with polyhedral or spherical unit cell geometry. Therefore, the extent to which the literature review, which mainly arose from liquid induced foam processes (soap froth), can be applied in the present case is questionable. As density increases, struts become thicker, joint regions become larger and cell walls are thick and mostly distorted. Plateau's laws are no longer present. Viscous stresses are responsible for

these large variations in the microstructure. However, such foams are used in a large spectrum of domains, from automotive products to advanced technologies. There is in fact a driving force to re-examine most of these products at all levels with the intention of making them lighter in a cost-effective manner while still performing the intended function or surpassing it. The challenge then becomes the introduction of the porosity in such a manner that the mechanical behavior is optimized for the considered level of density. In relation to this question, there is a whole section of current research based on controlling the morphological foam microstructure in order to achieve a certain level of performance. Computer-based modeling which respects as much as possible the morphological characteristics of these industrial foams would be of great help in this respect. We note that microstructural imperfections inherent to industrial foaming processes are present (Fig. 1) and may lead to variations in the mechanical responses.

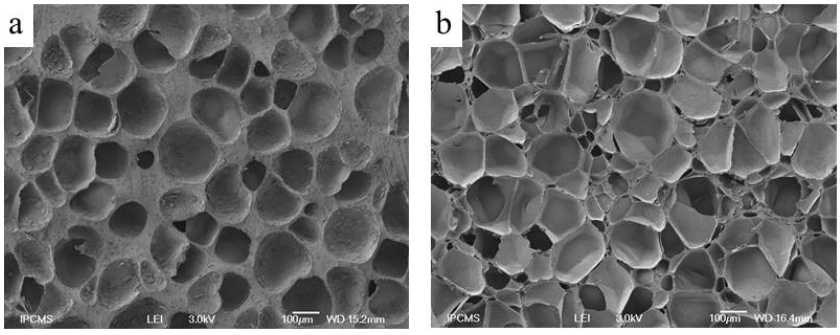

Figure 1: SEM observations of industrial elastomeric closed-cell foam microstructures of respectively (a) 58% and (b) 82% porosity. The cells shapes are neither circular nor polygonal and several imperfections inherent to the industrial process are present (holes in the cell wall).

For instance, the stiffness was observed to decrease by up to 40% when “wavy” cell walls (in opposition to “flat” cell walls) were taken into account in closed cell foams [8]. Other studies on the influence of cell shape variation (Grenestedt and Tanaka [9]) or of cell wall thickness variation (Grenestedt and Bassinet [10]) on stiffness response all concluded that it is necessary to incorporate the geometrical details of foam microstructure into the models to obtain valuable results. In order to do so, in the present study, an ad-hoc modeling of foam microstructural formation is described and allows for microstructural imperfections, as in those observed in real industrially made foam, to be taken into account. Given that bubble coalescence is not yet fully understood despite years of investigations [11], it is not our intention to detail all the chemico-physical mechanisms driving the foaming. In this context, Voronoi tessellations obviously do not involve any physical aspects such as gas diffusion

which are so essential to foaming. Nevertheless, there is no doubt that they are very useful to approach a characteristic microstructure of dry foam. The substantial idea is to obtain at the end a versatile microstructural topology that resembles the real ones at best and that can be further used as templates for mechanical studies.

To achieve realistic modeling, high resolution X-ray micro-tomography can also be used [12-16] but it is nevertheless not as straightforward as the microstructure generation-based modeling methods, since it corresponds to a fixed geometric representation of one foam microstructure. Here, to get an idea of the mechanical behavior, one must analyze the effects of all the individual parameters constituting the microstructure and morphology of the foam (cell size, cell shape, connectivity, spatial cell distribution). The task is not easy as these parameters may couple each other. Furthermore, one may not have at hand a sufficiently large variety of real polymeric foams carrying all possible microstructures and morphologies. Indeed, the foaming process is relatively complex to modulate and sometimes impossible to attain in order to obtain a variety of structures that would have the same given porosity but with different morphologies (cell size distribution for example). Consequently, we have preferred to develop a model that generates closed-cell polymeric foams inspired from a real manufacturing process. The model simulates the evolution of interacting cells in a polymer melt encompassing all the steps from the nucleation stage, where tiny closed-cells appear, expand and mature until the ultimate microstructure is obtained. Despite the fact that Ostwald ripening and possible coalescence of the cells are not fully taken into account, our model mainly gives an insight of the way cells interact when the nature and the distribution of the mixture are varied in order to obtain the ultimate geometry and shape of the cells (wet, dry…).

The model presented here particularly distinguishes itself from those already published by describing the radial fluid flow of the mixture during foam expansion. It combines spatial and temporal nucleation of cells and of gas therein that will form the cell structure. One of the main focuses of our model relates to the interactions between bubbles that grow and deform while they approach and encounter neighboring ones to ultimately lead to the complex microstructure of the foam. Our model, although based on a simplified vision of the foaming mechanisms, appears advantageous as it is more dynamic in the sense that it combines the radial flow of the mixture whereas the cells nucleate and grow at the same time, together with the gaseous release. The results demonstrate how polydisperse polymeric solid foams can be generated, and how close their ultimate morphology resembles the real ones measured by X-

ray microtomography at high resolution, using synchrotron radiation. These structures provide the basic geometry for calculating mechanical properties with the finite element method.

II. FOAM MODELING

II.1. Numerical implementation for foam microstructure generation

Polymeric foams are produced in a number of different ways. Examples are through slab-stock by pouring, extrusion and different forms of molding. In the work presented in this article, we have focused on one of the most widespread industrial processes based on chemical blowing agent (CBA). This process is usually comprised of three steps. First, thermoplastic polymer material and additives, such as carbon black, plasticizers and sulfur, are mixed together in the most homogeneous way. The second step consists of heating the polymer mixture up to the required temperature allowing the CBA to decompose and gas bubbles to be released. At this stage, cells nucleate. At last, the gas cells are observed to grow as the temperature is maintained with possible coalescence (ripening process). Then the temperature release stabilizes the cellular structure and leads to the ultimate morphology of the foam. The total volume expansion is quite large, a factor of about 10 being often encountered. This foaming process appears to be a very general common one in industry for polymer materials whether chemical reticulation is used or not (such as natural rubber, PVC, PE).

The mixture composed of the polymer material and the other components is in a solid state before the heating stage. Then, as the heating goes up to the melting temperature the mixture can be considered as a highly viscoelastic solid. Since the released gas is at a higher pressure than the atmospheric one, the created pressure gradient constitutes the main source of driving forces that cause the cells growth. In many polymer foaming processes the gas amount in each closed-cell is constant: this observation will credit the assumption taken in our model (see § II.1.1). The foam expansion creates temperature diffusion and convection phenomena in the melt. The temperature significantly influences the characteristics of the foaming process and the physical properties of the polymer melt such as the cells nucleation, the viscoelasticity and the conductivity. The elasticity of the polymer melt becomes particularly important with steep contraction or expansion in the flow direction [17]. The elastic modulus, E_T, is here considered to decrease exponentially with temperature, T:

$$E_T = E_0 \exp[a(T_0 - T)] \qquad (1)$$

with E_0 the elastic modulus at the initial temperature T_0. This phenomenological law is generally used in the vitreous regime of polymers, even if more complex models reflecting glass transition effects can be proposed [17, 18]. To describe the usual observation that fluids are less able to flow when the temperature decreases, the increasing viscosity of the polymer melt, η_T, is described as having an Arrhenius behavior [19, 20]:

$$\eta_T = \eta_0 \exp\left[\frac{E_A}{R}\left(\frac{1}{T} - \frac{1}{T_0}\right)\right] \qquad (2)$$

where η_0 is the viscosity at the initial temperature T_0, and R the ideal gas constant. The activation energy E_A characterizes the thermal plasticity of the material.

II.1.1 Single cell growth model

To start with, we first describe the expansion of an isolated bubble in an infinite medium by investigating the forces operating at the gas-melt interface. Then, we investigate the evolution of a multi-cellular system where the nucleation and the growth of different cells can occur simultaneously.

For an individual gas cell, the main interacting forces at the interface are the forces generated by the internal pressure in the cell, the reaction forces in the polymer melt and the surface tension forces. In the following these three contributions are defined:

- **Internal pressure**

Within the framework of the studied manufacturing process, as described beforehand, we may simplify by considering that there is no gas diffusion and that the quantity of gas inside the cell is constant (closed-cell foam). The gas (CO_2 or N_2) is modeled as an ideal gas. The Boyle-Mariotte law [21] is used as the temperature of the gas is also considered quasi constant (isentropic expansion). Note that this assumption is justified because there are very little thermal exchanges between the gas and the melt. The internal pressure creates a force directed in the normal direction $\vec{u}_r$ of the cell interface, located at a distance R at time t, towards the exterior (the mixture) and is inversely proportional to the volume:

$$P_{gaz}(R,t) = \frac{P_{in}V_{in}}{V(t)} \qquad (3)$$

where P_{in} designates the initial pressure of the compressed melt and V_{in} is the initial volume at cell nucleation.

- **External pressure in the polymer melt**

As soon as the pressure gradient created at the interface is set the system is no longer at the equilibrium and the matter moves progressively together with the bubble, which grows

concomitantly. The Kelvin Voigt rheological model has been adopted to describe the viscoelastic behavior of the mixture material, where material elements move in the melt treated as a continuum [22-24]. Despite its simplistic approach it is of interest as one may infer the main effects of the rheology on the morphology and structure of the ultimate polymeric foam. The properties of the melt are characterized by a dynamic viscosity η_T and a bulk elastic modulus K_T, both of them depending on temperature *T*. As the mixture is considered as incompressible (i.e. ρ =const), the movement of an elementary particle, spotted by its displacement vector, $\vec{u}$, and velocity, $\vec{v}$ (the material derivative of $\vec{u}$) is described by the Navier-Stokes equation:

$$\rho\left(\frac{\partial\vec{v}}{\partial t}+\left(\vec{v}.\vec{\nabla}\right)\vec{v}\right)=\rho\left(\frac{D^2\vec{u}}{Dt^2}\right)=\vec{\nabla}.\bar{\bar{\sigma}} \qquad (4)$$

where $\bar{\bar{\sigma}}$ designates the stress tensor. Note that normally the Navier-Stokes equation is written with a pressure gradient (that is needed to maintain incompressibility) separated off from the viscous (or viscoelastic) stress. In equation (4) the pressure term is nevertheless implicit in the stress tensor where pressure and surface tension contribute (see eq. 10 below). Here the adopted equation presentation allows the three components to be separately decoupled in the movement equation in order to emphasize the role of the stress fields inducing the cell expansion.

The stress tensor is related to the strain tensor, $\bar{\bar{\varepsilon}}$, and its rate, $\dot{\bar{\bar{\varepsilon}}}$:

$$\bar{\bar{\sigma}}=K_T\bar{\bar{\varepsilon}}+\eta_T\dot{\bar{\bar{\varepsilon}}} \qquad (5)$$

coupled with the particle displacement:

$$\bar{\bar{\varepsilon}}=\frac{1}{2}(\vec{\nabla}\vec{u}+\left(\vec{\nabla}\vec{u}\right)^T) \qquad (6)$$

In the following the projection on the radial direction is considered. Since spherical waves are expected, and one uses the variable change $\overrightarrow{\sigma'}(r,t)=r.\vec{\sigma}(r,t)$ with *r* redefined as the radial distance from the interface. Using the approximations detailed in Appendix, the stress field $\vec{\sigma}(r,t)$ in the mixture obeys the differential equation:

$$\frac{\partial^2\sigma'}{\partial r^2}-\frac{1}{c^2}\frac{\partial^2\sigma'}{\partial t^2}+\frac{\eta_T}{K_T}\frac{\partial^3\sigma'}{\partial t\partial r^2}=0 \qquad (7)$$

where *t* is the time variable and *c* represents the speed of propagation of the perturbation in the fluid mixture. Its expression, $c=\sqrt{\frac{K_T}{\rho_0}}$, shows its dependence with the elastic bulk modulus of the mixture K_T and its mass volume (density) ρ_0. Equation (7) appears almost equivalent to the equation describing the sound propagation in a viscous and incompressible medium [25]. The first two terms describe the space-time d'Alembert propagation of a wave

[26] whereas the third term describes the damping and attenuation effects due to the viscoelastic character of the mixture. One solution of the stress field, $\vec{\sigma}(r,t)$, with the origin r=0 taken at the interface is given by:

$$\vec{\sigma}(r,t) = \left[P_{ext} + (P_{in} - P_{ext})\frac{r_{nuc}}{r+r_{nuc}} e^{-r/\delta} e^{-t/\tau}\right] . \vec{u}_r \qquad (8)$$

where $\delta = \frac{4\eta_T}{\sqrt{\rho_0 K_T}}$ represents a spatial screening length and $\tau = \frac{\eta_T}{K_T}$ a time decay, both related to the characteristics of the mixture, and r_{nuc} is the cell radius at nucleation (fixed value considered independent of time). As expected the solutions are spherical waves propagating away from the bubble with a magnitude decreasing as the inverse of distance (the time oscillations contribution has been omitted and eq. (8) represents the envelop of the wave). The screening length is characteristics of the mixture and describes the absorption of the overpressure wave. With typical values of ρ_o = 2000 kg/m^3 for a polymer melt with an elastic bulk modulus K_0 =10^9 Pa and viscosity η_0 between 10^{2}Pa.s and 10^3 Pa.s at the processing temperature of the order of 200 °C, the damping spatial characteristic length δ is of the order of 500 µm; it will increase by a factor 3 at the end of expansion since both rigidity and viscosity would have increased (η_T between 10^4 and 10^5 Pa.s and K_T of the order of 10^{12} Pa). Concerning the temporal damping, τ, it is of the order of 1 µs, underlying that the rate limiting step is due to bubble expansion after the gas is already in the bubble, rather than mass transport of gas into the bubble, in agreement with real polymer foaming process where no gas diffusion occurs over the expansion process lasting no more than fraction of a second.

- **Surface tension forces**

The surface tension γ generates the elastic tendency of a fluid surface to acquire the least surface area possible. The force at a given point M on the cell interface acts along the normal $\overrightarrow{n_M}$ of the interface (oriented outwards) and its magnitude is given by the Young-Laplace equation [27]:

$$\overrightarrow{\Delta T}(M) = \pm\gamma\left(\frac{1}{R_1} + \frac{1}{R_2}\right)\overrightarrow{n_M} \qquad (9)$$

where R_1 and R_2 are the principal radii of curvature at M (considered as algebraic values). The surface tension forces are directed inwards or outwards depending on the sign of the mean curvature.

The resulting stress $\vec{\sigma}_{eqM}(M,t)$ acting on an elemental particle interface centered at point M, is the sum of these three terms calculated at point M:

$$\vec{\sigma}_{eqM}(M,t) = P_{gas}(R_M,t)\vec{n}_M + \vec{\sigma}_{ext}(R_M,t) \pm \frac{2\gamma}{R_M}\vec{n}_M \qquad (10)$$

where $\vec{\sigma}_{ext}(R_M, t)$ is the external stress per unit area applied by the material mixture at point *M*. The displacement of the interface of the cell can thus be deduced.

II.1.2. Multi cellular growth model

- **Stress field in the melt**

In the single cell model, the polymer melt undergoes a stress field generated alongside with the cell growth. The latter is isotropic and hence the resulting stress field is radial pointing toward the outer of the cell (the total hoop stress is zero as the resultant of the lateral forces cancels). In the multicellular model we assume that each cell creates a stress field identical to the one inferred by the single cell model. However because the cells will encounter neighboring ones as they grow they will get deformed and their interface will not remain spherical. Isobaric lines are no longer concentric circles but depend on the morphology of the expanding structure. The distance from a point *M* in the melt to the cell interface *i* is noted di_M. At the interface *i,* the elementary quantity di_M is zero and in the melt $di_M > 0$. Finally, the total stress field in the melt is the sum of the resulting stress fields caused by the *N* gas cells taken separately:

$$\vec{\sigma}_{tot}(M, t) = \sum_N \vec{\sigma}_{ext-i}(di_M, t) \qquad (11)$$

Note that the additivity of the stress fields from each individual bubble taken in isolation is an approximation valid at first order only, since the individual stress field decays exponentially with the distance from the cell interface (see eq. 8).

- **Temporal distribution**

The multicellular growth model must incorporate the cell nucleation distribution over time knowing that their growth and nucleation may happen simultaneously. Following other works [28] a configurable normal distribution is adopted to give different nucleation rates:

$$N_c(t) = N_0 - N_1 \frac{e^{-bt_1{}^2}}{1-e^{-bt_1{}^2}} + \frac{N_1}{1-e^{-bt_1{}^2}} e^{-b(t-t_1)^2} \qquad (12)$$

The number of cells $N_c(t)$ nucleated at time *t* depends on the number of cells N_0 that were initially nucleated before the foam expansion, but also on the maximum number of additional cells N_1 nucleated from 0 to time t_1, and on the standard deviation of the distribution, represented through the constant *b*. It is considered that no more cells are nucleated after t_1, so eq. 12 is valid for $0 < t < t_1$. We will see further that several types of distribution can thus be obtained: no additional nucleation (distribution 1; b=infinite; see Fig. 3 left); additional

nucleation with no delay (distribution 3; b=0.013 in (time iteration unit)$^{-2}$; Fig. 3 right) or with delay (distribution 2; b=0.047 (a.u)$^{-2}$; Fig. 3 middle)

- **Spatial distribution**

In our model we assume that all the cells nucleate with an initial fixed radius and identical internal pressure. We have developed a homogeneous nucleation model that incorporates the concept of influence volume approach (IVA) around the cells [29]. Each cell has an influence on a zone surrounding it. The IVA is a band around each cell surface. In most cell growth models this zone is intended to provide an accurate measure of the amount of gas entering into the cells. It changes over time depending on the gas concentration in the vicinity of the cells. However, for the studied foam manufacturing process, there is no in-flux gas diffusion directed from the polymer melt toward the cells. Off gassing is generated within nucleating and blowing agents and for each cell the whole compressed gas inside is solely generated at its nucleation stage. There is also no gas diffusion outward the cell since we consider the process of closed-cell foam only. In the influence zone of each cell we consider that no cell nucleation may occur; in other words no additional cell may merge or coalesce with the largest cell already in place. This description has a physical meaning as stress field around a bubble is intense and prevents cell nucleation; moreover it is known that small bubbles may be sucked by larger ones (Ostwald ripening). The extent of this zone is determined from the characteristic properties of the polymer melt and the process conditions. It has therefore an identical and constant spatial extent value for all the cells regardless of their size. Figure 2 is a 2D illustration of the cells spatial distribution depending on IVA.

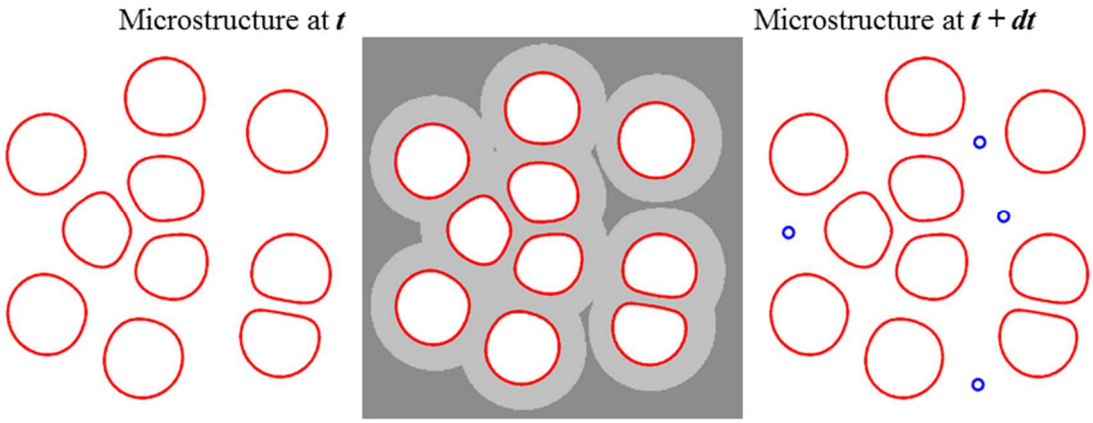

Figure 2: Illustration of the two concepts on which the model for interacting cells is based. Every cell (contour drawn in red) creates an influence zone in the melt (grey) surrounding it. As a result the nucleation of new

additional cells (in blue) may occur only away from this restricted zone. As time elapses, the already nucleated cells grow and expand in the melt and the potential nucleation zone (in black) shrinks.

The potential zone of nucleation at a given time *t* is the virtual volume in which new cells nucleation can occur. The number of cells is given by the nucleation time distribution whereas the locations of their centers are determined according to a random selection algorithm which allows both homogeneous and heterogeneous nucleation to be modeled. These terms refer to simultaneous nucleation of cells or not, leading to monodisperse or polydisperse structure respectively (see next section).

II.2. Resulting foam morphology

The stress fields calculated are based on a 3-D point of view (see Appendix). But the same principle can be applied in 2D; therefore the simulation algorithm was implemented in 2D and 3D. We chose the Eulerian approach. Since the nonlinear partial differential equations and boundary conditions are already solved, the stress field in the mixture (equation 8) and the displacement of the cells interface (equation 10) are simply calculated via a numerical grid. The latter is a discrete representation of the geometrical domain on which the numerical simulation is carried out. We have taken a square grid (cubic grid in 3D), defined by its pitch size (LxL) and by the number of elements N^2. The position of each node of a grid element is given by its coordinates (i,j). The vectorial stress field is calculated at each node.

The evolution of the gas-mixture interfaces is monitored by means of a mesh composed of interconnected points that describe those interfaces. Every point models a material particle of the mixture at the interface. An adaptive resolution sets the spacing between points following the contour of the cells in order to maintain the same precision in their output all along the cells growth. This is a re-meshing. Thus, if necessary, the algorithm may remove or conversely add some points in a given cell depending on its evolution throughout its growth. In 3D we use 642 points per cell constituting a triangular mesh.

Some microstructure characteristics such as the mean cell volume, the mean equivalent cell diameter and porosity are calculated. In the simulation the cells can move continuously. An equilibrium state is assumed to be reached when the change in foam porosity no longer evolves (with variation smaller than 0.01%). The simulation is then stopped leading to the ultimate microstructure. The morphometry of the obtained foam at equilibrium can be characterized by two inferred parameters, the porosity, *P*, and the dispersion coefficient of the

cell size, C_{vol}, defined as the dimensionless ratio between the standard deviation and the mean area A_m (simulation in 2D) or volume (simulation in 3D) of the cells: $C_{vol} = \frac{\delta_A}{A_m}$.

Following we present and discuss some simulation results in 2D and 3D.

II.2.1. Generation of 2D microstructures

Different microstructures morphology can be generated by varying the spatio-temporal distribution of the cells, the process parameters and the polymer melt characteristic properties. Indeed, because K_T and η_T affect the distance scale δ and the time scale τ differently, the distribution of cell size will depend on the ratio of τ to the distribution of nucleation times, and the ultimate morphology will depend to whether it is the variation of K_T or η_T which dominates. Figures 3 to 5 provide several examples of 2D microstructures containing each 100 cells and characterized by four parameters: two input parameters which are the screening distance δ and the surface tension γ_0 and two measured parameters inferred from the final microstructure: the porosity P and the dispersion coefficient C_{vol}. Excepted for the temporal nucleation and the two input parameters aforementioned all microstructures have been obtained with the same characteristic properties. In the microstructure morphologies of Fig. 3 the screening distance δ has been kept to the same value 90 µm but the time dependence of the cell nucleation has been varied. Thus, when a simultaneous cells nucleation (type 1 distribution) is chosen the obtained microstructure is close to monodisperse, i.e constituted of nearly identical cells in size and the coefficient C_{vol} is very small. When the cells nucleation is operated with delay (type 2 distribution), a polydisperse microstructure is obtained with large values of C_{vol}. Thus the microstructure is constituted of two distinct scales of cell sizes and the coefficient C_{vol} is larger than 1. A temporal nucleation of microstructure following a Gaussian distribution leads to a polydisperse microstructure with $C_{\mathrm{vol}} = 0.44$. Note that the measured porosity P is almost the same for these 3 microstructures ($P = 85 \pm 1$ %), despite very different microstructure morphologies and cell size distribution. The small variation for the reached value of porosity is linked to the incremental time step used in the computing calculation. This already indicates that the foam porosity cannot be alone a relevant parameter to describe the cellular microstructure (see also Discussion).

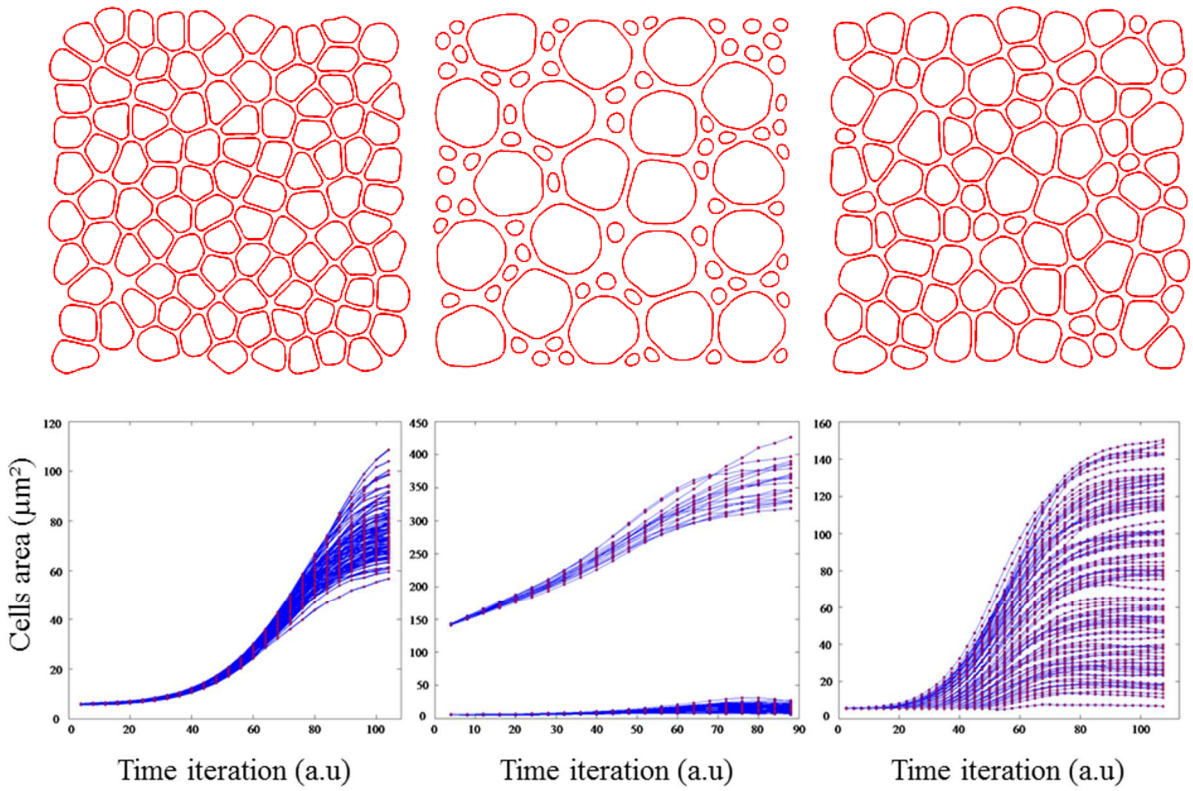

Figure 3: 2D microstructures generated for different time distribution profiles for the cells nucleation. In these simulations all other parameters were kept constant (screening length δ = 90 µm; surface tension γ_0 = 15 mN/m). Note the overall porosity is used as convergence criteria, here P = 85 ± 1 %. Quasi-monodispersity is observed only when the cells nucleate simultaneously (type 1 distribution; left) and C_{vol} = 0.14. Otherwise C_{vol} = 1.63 > 1 when cells nucleate with delay (type 2 distribution; middle) with two marked populations of cell sizes; and C_{vol} = 0.44 when the nucleation follows a Gaussian temporal law (right). Note the different expansion scales for the growing cells.

To get insights into the influence of the screening length, we have generated microstructures where all cells nucleate at the same time, namely at the starting time of the simulation (type 1 distribution). Therefore all the cells reach nearly the same size and the C_{vol} has a low value (Fig.4). These microstructures differ by the wall thickness separating consecutive cells. The porosity P decreases as δ increases.

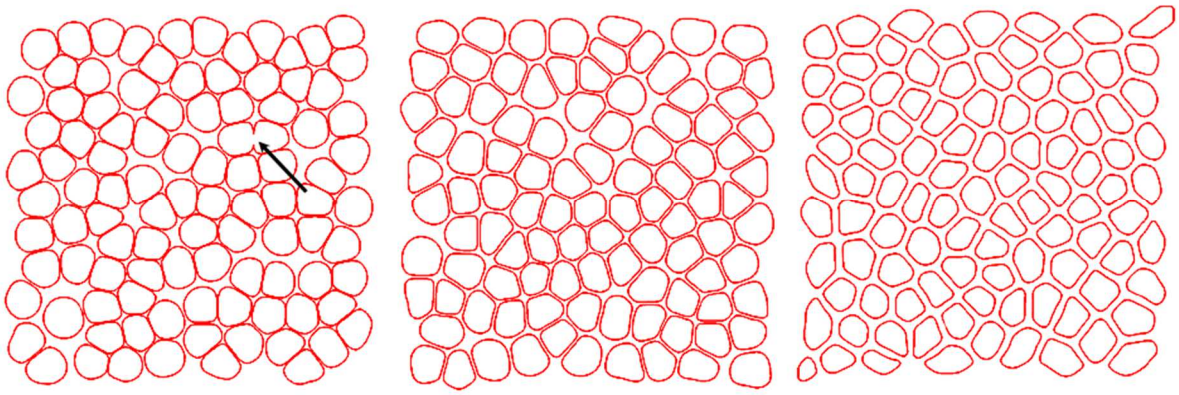

Figure 4: Influence of an increasing screening length, δ, on the 2D microstructures generated when all cells nucleate simultaneously (type 1 distribution of Fig. 3), all other parameters being kept constant. The obtained porosity, P, decreases and the polydispersity in cell sizes, C_{vol}, slightly increases but still remains small. *Left*: δ = 56 µm, P = 90%, C_{vol} = 0.08; *middle*: δ = 76 µm, P = 85%, C_{vol} = 0.12; *right*: δ = 133 µm, P = 72%, C_{vol} = 0.16. Note that an event of two encountering cells leads to their coalescence as illustrated by the arrow.

The influence of the surface tension has also been investigated. All microstructures in Figs. 3 and 4 have the same surface tension coefficient γ_0 while the microstructures in Fig. 5 were calculated with a surface tension $1.6\gamma_0$ and with $2\gamma_0$ (with a screening distance δ kept fixed). As expected, when the surface tension increases the cells become more spherical and are smaller. Indeed, by minimizing the cell surface energy the surface tension forces generate constraints facing cells growth. These constraints depend on the curvature of the cells contour, which results in a rounding of the cells shape. The apparently strong influence of the surface tension might be associated with the non-Newtonian behavior associated likely to the fact that the Kelvin-Voigt model describes a viscoelastic solid.

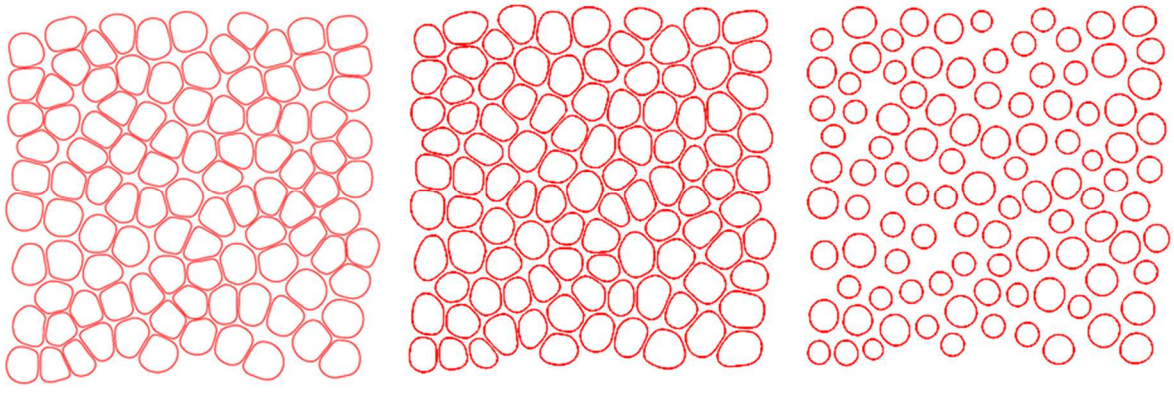

Figure 5: Influence of an increasing surface tension, γ, on the 2D microstructures generated when all cells nucleate simultaneously (type 1 distribution of Fig. 2), all other parameters being kept constant (screening length δ = 70 µm). The obtained porosity, P, decreases and the polydispersity in cell sizes, C_{vol}, increases. *Left*: $\gamma = \gamma_0$, P = 86%, C_{vol} = 0.10; *middle* : γ = 1.6 γ_0, P = 85%, C_{vol} = 0.16; *right*: γ = 2.0 γ_0, P = 47%, C_{vol} = 0.29.

II.2.2. Generation of 3D microstructures

The algorithm in 3D is an extension of the 2D one. Generating an accurate 3D structure depends on the initial sampling points defining the surface of the cells and the surface meshing adopted. Each cell at nucleation is represented by a polyhedron with a set of equidistant vertices. A regular mesh of these vertices with equilateral triangular elements is adopted to form the spherical polyhedron delimiting the contour of each cell. The obtained microstructures after each numerical simulation are vector images (Fig. 6a). The corresponding models are then extracted. In 3D the microstructure simulation gives a 2D triangular meshing of the cells surface (Fig. 6a). The cells are solid materials redefined then by their surface contour (Fig. 6b). Finally the bulk material is extracted from the volume outside the cells (Fig. 6c). Some samples are extracted by cutting cylindrical or cubical shapes to get the final microstructure models. This procedure has allowed us to generate a large variety of microstructures with different morphologies in terms of porosity and polydispersity. These morphologies are geometrically similar to the real observed microstructures [16] as we will discuss in the discussion section (§ IV).

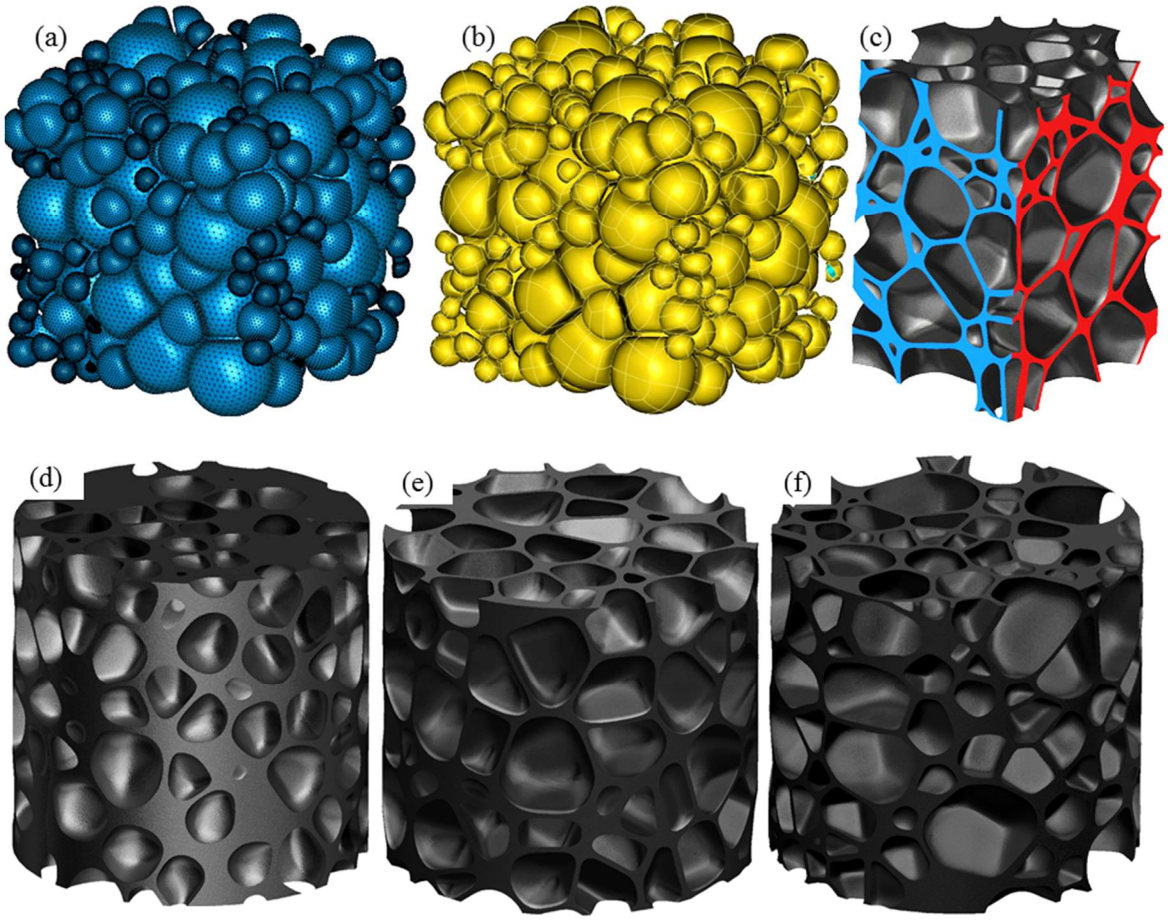

Figure 6: Reconstruction of a 3D microstructure. After having obtained the cellular structure by numerical simulation (a), the contour surfaces of the cells are created (b) from which the microstructure is extracted (c); see main text. Different porosities and polydispersities can thus be generated: (d) $P = 59\%$, $C_{vol} = 0.35$; (e) $P = 73\%$, $C_{vol} = 0.33$; (f) $P = 75\%$, $C_{vol} = 1.37$.

II.3 Sources of errors and limitations of the model

It is important to investigate the errors and the limitations of the physical model in order to validate the consistency and to compare the generated microstructures to the real ones encountered in polymeric foams. Numerical simulation of the microstructure evolution during the foam manufacturing process is only an approximate solution. In addition to errors that could be introduced in the development of the physical model algorithm, in its programming or in the implementation of boundary conditions, the final numerical solution includes several types of systematic errors [30]:

- Modeling errors due to a discrepancy between the genuine foam manufacturing process and the exact solution of the physical model even if the latter is derived without any approximation. This aspect is detailed in the Discussion section.
- Approximation errors/discretization errors due to a finite spatial and temporal resolution.

The smallest element dimension in the simulation grid, L_{min}, must be chosen so that any wall thickness contains enough elements. Since the spatial screening δ is a dimensional characteristic of the microstructure walls, an upper bound of L_{min} is given by: $L_{min} < \frac{1}{3}\delta$ where $\delta = \frac{4\eta_T}{\sqrt{\rho_0 K_T}}$.

The effect of the grid mesh size on the resulting value of the spatial screening length δ was controlled running a simulation of two growing bubbles (Table 1). As the grid pitch size is approaching the upper bound limit, the spatial resolution becomes too low to get accurate values (stability of the result is not maintained).

Grid size (Px)	δ (Px)
34x34x34	3.0445
50x50x50	3.1837
100x100x100	3.1816

Table 1. Accuracy of the δ value for different grid sizes (100^3, 50^3, 34^3)

The approximated solution of the stress field in the melt has a specific domain of validity (see Appendix). Here ones consider that the particles move with small displacements and at low velocities: thus, the discretization time Δt must be smaller than L_{min}/c, where c is the

propagation speed of the perturbation in the fluid mixture. It constitutes the criteria we chose for the maximum time step. This inequality sets an upper bound for the time increment of the simulation ($\Delta t < \frac{\eta_T}{K_T} = \tau$, where τ is the time decay), beyond which the approximations used for equation (7) are no longer valid.

III. MECHANICAL PROPERTIES

III.1. Finite element modeling

To check for the performance of the "ad-hoc" modeling under study, a microstructural model was developed from the basis of structural analysis by x-ray tomography of real elastomeric foam of 62% porosity. Then a comparison of the compressive mechanical behavior between the model microstructure and the real foam was performed. This approach is often observed in the literature review dedicated to foam modeling. As an example we can quote the work done by Jang *et al.* for open-cell foams [31]. In our particular case, considering the bubbles size as indicative of their lifetime, a nucleation rate with time was chosen as input parameter for the simulation to be run. This goes with the determination of the time distribution profiles for the cells nucleation. Then the seed points were chosen to appear randomly and the overall porosity stated the termination criteria for the simulation. The physicochemical characteristics of the materials were provided by our industrial partner and physically reasonable values for the mechanical properties were used (K_0=10^{12} Pa, η_0=10^3 Pa.s, γ_0=15mN/m). For this material input, one of the difficulties in determining precise values is due to chemical blowing agents that are exothermic when they decompose at high temperature. This may induce chemical reactions during the process. The process generates a cellular microstructure that is closely representative of actual polymeric foam microstructures as demonstrated in the discussion section here after, for a same kind of foam although with a little lower porosity. The finite element program MSC Marc was employed to perform numerical compressive tests within the framework of the large displacement theory. The results were compared to experimental measurements carried out on five polymeric foam samples. These experimental tests were performed at ambient temperature under constant displacement rate using an INSTRON E3000 testing machine equipped with a 1kN load cell. The constitutive model chosen for the base material was determined using a Mooney Rivlin fit of the engineering tensile/compressive stress-strain curve of the bulk material (not foamed). One can report to the Supplementary data document for details. A model containing a large number of cells (587 cells) was chosen as representative volume element (RVE). The size of this RVE was

carefully established in our previous work [12]. It is also in good agreement with several previous studies [32]. A standard model contained around $1.5.10^6$ elements and each simulation took about 74h of CPU time on a workstation with 128 Gb of RAM. The compressive response was also compared to predictions obtained with periodic unit cells of spherical voids arranged in FCC or BCC structures and for the Kelvin's structure, while keeping the same level of porosity (62%). Figure 7 shows the different microstructural morphologies used for the mechanical study. Note that ad-hoc modeling presents microstructural morphologies that are the closest to the ones observed in real polymeric foams for the same level of porosity (Fig. 1a).

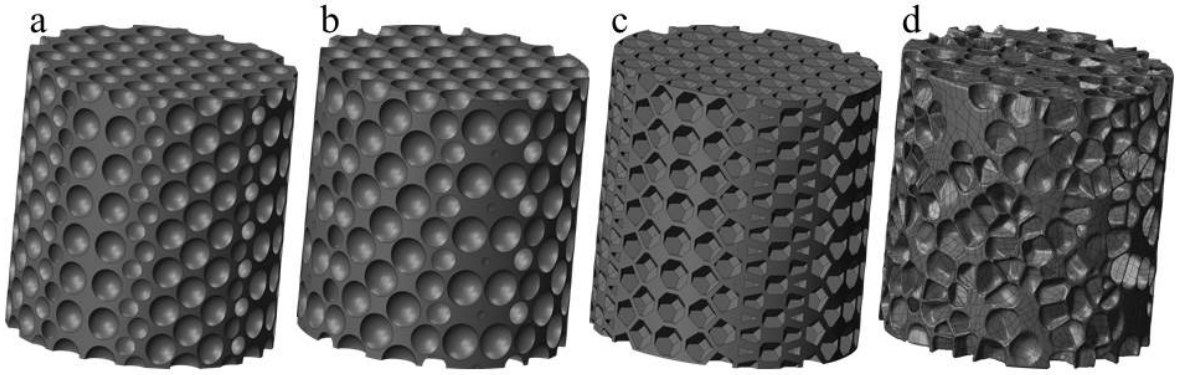

Figure 7: Sketch of the numerical models, from left to right: a) Body-centred cubic (BCC), b) Face-centred cubic (FCC), c) Kelvin's tetrakaidecahedron structure d) "ad-hoc" model.

III.2. Compressive behavior

Figure 8 shows the compressive stress-strain curve obtained for the numerical models in comparison to the measurements led on the industrial foam for a porosity of about 62%.

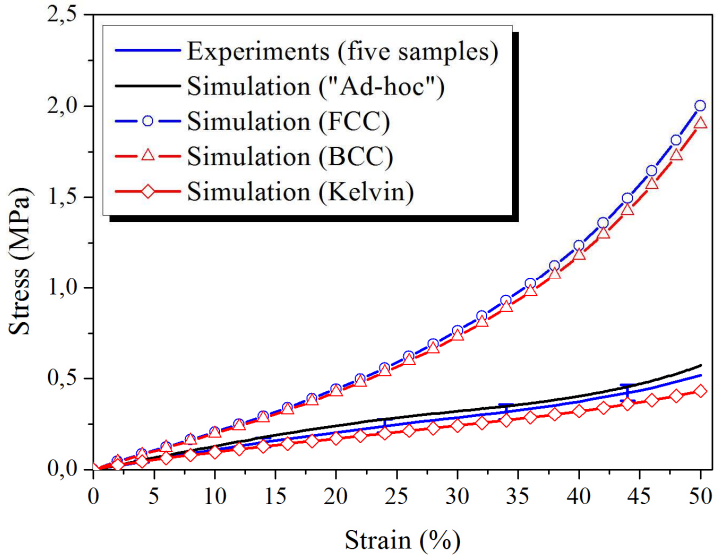

Figure 8: Large strain compressive behavior of foams – comparisons between numerical models and experiments

The values reported for the porosity are the ones calculated directly from the meshing element volume. Thus, small differences can be observed within 1% of the theoretical targeted value even if the mesh size was fine enough to represent accurately the geometry. The prediction by means of the ad-hoc modeling is the closest to the one observed experimentally. In opposite, models based on ordered spherical voids overestimate the properties and seem inappropriate to represent real foam behavior, while the one based on Kelvin's cell tends to return to the true response. The reason for these observations can be inferred from consideration of the structure of the interstitial material that may present strain localization in case of polygonal structure (ad-hoc and Kelvin) and thus diminishes the mechanical resistance of the foam.

The relative Young's modulus (E_{foam}/E_{solid}) for the considered crystalline arrangements of voids are in good agreement with model predictions of Christensen et al. [33] and of Heitkam et al. [34] with relative Young's modulus of 0.19. However, these predictive models and the scaling laws by Gibson and Ashby [35] fail to describe the experimental stress-strain behavior. As demonstrated by Heitkam et al. [34] Young's modulus for porous materials strongly depends on the porosity but it is much less affected by the way how the porosity is distributed. However, they also remarkably demonstrated that values of the Young's modulus are depending on the orientation of the applied load on the structure. To put it in another way, the dominant structural feature of the void materials is all about the necks confined between three or four voids. When they become narrowed because of high porosity or because of local topology distortion, a rigidity loss is observed. This explains the large difference observed when realistic foam microstructure simulation is considered since then very thin cell walls are randomly distributed inside the material leading to easiest distortional deformations as shearing or bending. Consequently, to accurately predict mechanical behavior, the distribution of material along the strut has to be taken into account and a FE simulation with close to exact geometry of the cells is needed. Scaling laws derived from beam theory proposed in the literature stay consistent with high void fraction when very thin interstitial material is assumed to be ideally and uniformly distributed into either struts or in cell walls of uniform thickness. We checked for the reproducibility of the results given by the "ad-hoc" modeling, by running another model with the same parameters (leading to a same C_{vol} and porosity). This model is reported in the Supplementary data document. Remarkably it leads to a compressive response very close to the one shown here.

IV. DISCUSSION

Establishing the relationships between properties and structure is a challenge for cellular materials, since the heterogeneous character of their complex morphology cannot be put aside. As a consequence a precise description of the microstructure of the polymer foam at all the spatial scales encompassing the mesoscopic and the micrometric scales is called for. The variety of morphometries encountered in polymeric foams results from a subtle interplay between thermal, physico-chemical, and rheological couplings during the foaming manufacturing process. In our work we have developed a simple physical model that generates closed-cells polymeric foams following the three steps of the most widespread and used industrial process based on chemical blowing agents. In particular we have proposed an original description of the expansion step during which the growing gas cells may interact, encounter, and eventually coalesce with neighboring ones, whereas simultaneously other and additional cells may also nucleate. The advantage of our model is its combination of thermodynamic and dynamic approaches. Here we discuss the validity of the physical based model and set some limitations.

One way of getting a flavor about the consistency of the microstructures generated by numerical simulations is to compare them with the real ones. In a previous work we showed how the complex microstructures of genuine polymeric foams can be determined experimentally with accuracy. To achieve this goal we used both electron microscopy and X-ray microtomography at high spatial resolution [12]. In Figure 9 the microstructure of closed-cell polymeric foam with a 56.0% porosity is compared with a simulated one generated with time distribution close to type 3 for the cell nucleation that lead to a similar value for the porosity (58.5%). Using the cells sizes as inferred from x-ray tomography data, the bubbles lifetimes can be estimated; as a consequence a nucleation rate with time can be defined. In the 3D view one must not attach too much importance to the fact that the outer cells appear different. Indeed as explained in details in [12] a cylindrical subvolume of the computed microtomography dataset is extracted from the final reconstructed image represented by a 3D array of voxels. As a result no periodic boundary conditions can be applied as they would be inadequate. Conversely, in numerical simulations the cells grow very quickly in the absence of external constraints. Therefore to overcome this discrepancy and minimize edge effects, we have extracted a Representative Elementary Volume (REV) with 400 cells at the end of the simulation. The spatial distributions of the cells for the experimentally determined and numerically simulated microstructures appear very similar as illustrated in the longitudinal sections. The quantitative statistical analysis on the cell volume shows also a very good

agreement (Fig. 10a). However, one can note small differences in the longitudinal sections (as outlined by the arrows in Fig. 9). Thus, the numerical simulation sometimes generates cells with a shape slightly more convex or rounded (green arrow, Fig. 9). Although the simulated microstructure is actually driven to the same porosity as the real foam, one can note that the ultimate porosity of the generated microstructure may depart slightly of the desired goal. The small discrepancy results from a rate of change of the cells volume during iteration and a porosity variation when the cylindrical microstructure sample is extracted. Another feature seen in simulation is the occurrence of a few spots where a large cell has replaced a couple of smaller ones as compared to the real microstructure (red arrow). Although these events are rare statistically their occurrence explains the small differences observed in the distribution of the cells volume. Thus, the microstructure generated by simulation has a 58.5% porosity slightly larger than that of the real polymeric foam (56.0%): as a consequence the mean cell volume is slightly larger (8289 μm^3 compared to 7668 μm^3). Here the mean cell value is calculated without considering the bubbles that may sit at the outer boundary. In order to correlate volume and shape for the cell distributions, a useful representation is in terms of sphericity, defined as the surface area of a sphere, enclosing the same volume V as the 3D object, divided by the surface area A of the 3D object: sphericity = $(36\pi V^2)^{1/3}/A$. The sphericity is in the range 0 to 1 with the upper bound reached only by a genuine sphere. As shown in Figure 10, the largest a cell, the most spherical. Indeed, the largest cells are often the oldest ones. During the expansion of the foam all the new nucleated cells appear around these large cells. The interactions between the cells deform the walls, but the large and old cells keep their very symmetrical shape and hence are more spherical. In other words, the larger the bubbles are, the more the strain field around them. This is why large bubbles are more spherical than the small ones, which deform more easily despite the surface tension. This observation is not induced by drawback of the numerical calculation or by some measurement uncertainty. The same effect is also observed when one analyzes the structure of real polymer foams as seen by X-ray tomography (Fig. 10). Figures 10a and 10b show the very good agreement between the two microstructures whatever the sphericity is plotted as a function of the cell volume or its equivalent diameter. But still, there are some slight differences: at equal sphericity, the cell size of the real microstructure is larger. This is particularly noticeable on the representation with equivalent diameters. Another way of analyzing the data is to compare the states at equal volume and equal equivalent diameter. Thus the cells in generated microstructures appear more spherical. The slight shift in their distribution toward higher values of sphericity indicates again that the numerical calculation generates cells with a more

rounded shape than that they have in reality, as also revealed by the longitudinal 2D sections of the microstructures (Fig. 10). These results underline that the cell volume fraction, that is the foam porosity, cannot be alone a relevant parameter to characterize a cellular microstructure. The position, shape, and orientation of all cells must be described. In addition, the topology, which is the position of all polymeric nodes and number of branches connecting the cells, and the distribution of cell walls thicknesses must also be determined. Provided these distributions to be assessed, one then will be on the route of relating properties with the structure of the polymeric closed-cell foams.

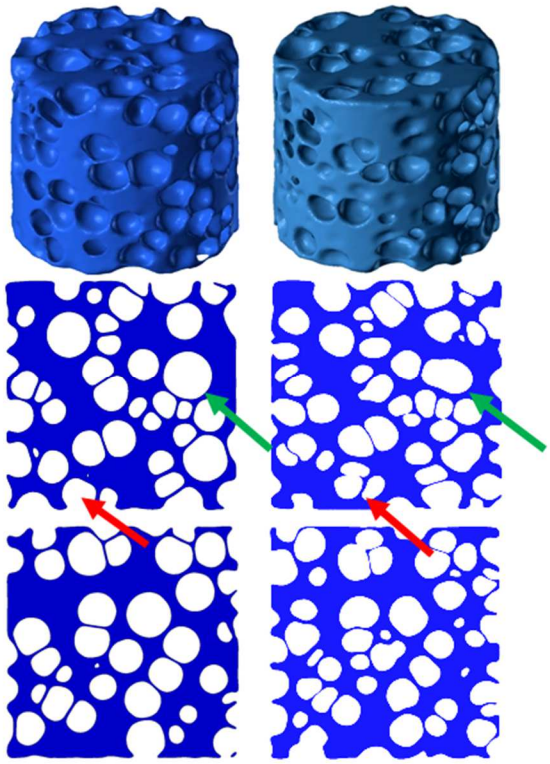

Figure 9: Comparison between a microstructure generated by numerical simulation (left, P = 58.5%) and a polymeric closed-cell foam measured by X-ray microtomography at high spatial resolution (right, P = 56.0%). Height/diameter is of 1.2 mm. *Top*: 3D reconstruction. *Bottom*: Two longitudinal sections emphasizing the close agreement between the respective spatial distributions of the cells in terms of their position, shape, and orientation, despite a few discrepancies outlined by the arrows.

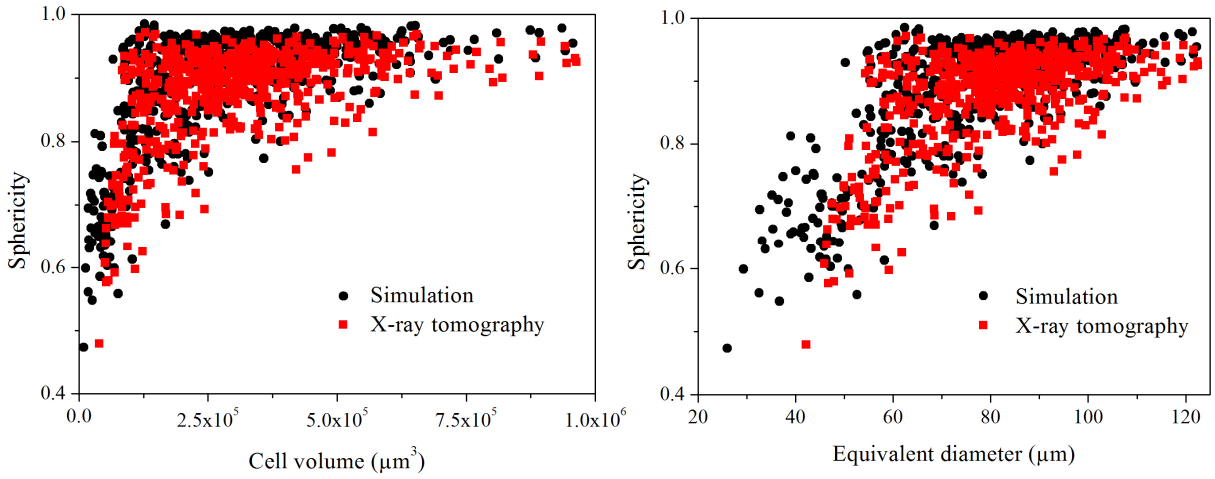

Figure 10: Sphericity and equivalent diameter distributions for the cells of the microstructures generated by numerical simulation (black) and compared to real polymeric closed-cell foams (red) of same porosity (cf. Fig.9).

The suitability of X-ray microtomography specification of real, complex foam microstructures demonstrates its use and importance for validating our physically-based model and numerical calculations. Given significant confidence in these calculations since a good agreement between the generated and the real microstructures is obtained, several remarks may be made regarding the assumptions set in our model. It is clear that having developed a dynamic approach, despite its limitations, is an asset. In particular, as the nucleation of cells, their growth through gas expansion, and the interactions between growing cells are taken into account simultaneously, more realistic microstructures of the cellular material are generated, and this, over a large range of porosities (from a few to 95 percents). The morphometry parameters correspond closely to the ones of real polymeric foams in terms of porosity, polydispersity, cell shape, anisotropy and orientation of the cells, wall thicknesses. Some descriptions of these parameters and subsequent comparisons are given in the Supplementary data document besides this paper. Thus three main parameters govern the ultimate microstructure of the cellular material. The screening spatial length of the stress field will typically determine the thickness of the cell walls of the ultimate microstructure. The surface tension at the interface between the gas cell and the polymer melt will govern the shape and anisotropy of the cells. The time distribution of the cell nucleation will determine the porosity, anisotropy, and polydispersity of the ultimate foam. In this work we examined three main classes of temporal distributions as the instants of the cell nucleation are unknown experimentally. However, these instants are correlated with the cells size distribution if one assumes that the older the cells the bigger they are. Since the structure of the real foam microstructure is polydisperse one may assume that each cell adopts a unique growth profile.

Using our X-ray tomography measurements, the lifetimes of bubbles were estimated from the cells sizes. The time distribution profiles for the cells nucleation were chosen accordingly (Gaussian temporal law). Additionally, the barycenters of the cells inferred from the x-ray tomography data define the nucleation locations of the bubbles. For the materials input, the parameters were discussed with our industrial partner. It has been pointed out that the properties of cell walls of polymeric foam may differ from that of the bulk material from which the foam is made, due to polymer chain alignment during foaming processes and chemical changes by the addition of foaming agents. It is thus very difficult to reproduce samples of exactly the same material nature as the one of the cell walls. Also, it is usual that more than ten different chemical components are present. For these reasons, we used a bulk modulus of $K_0=10^{12}$ Pa, a viscosity of $\eta_0=10^3$ Pa.s and a surface tension of $\gamma_0=15$mN/m which are physical reasonable values. As already stated, the overall ultimate porosity was chosen as termination criteria. The effectiveness of our method is based mainly on the assumption that the centers of the already nucleated cells do not move during the foaming process. Refinement of the temporal distribution of the cell nucleation is in progress but yet we note that they have already led to a very good description of realistic polymeric closed-cell foams. Remarkably, it also appears that the strong assumption of incompressible polymeric material has not induced strong drawback in the results. The development of the present physical model algorithm is not made without simplifications. All along the description of our model, we have underlined what are the framework and the limitations. Beyond the simplifications, the complex chemico-physical mechanisms driving the foaming process have not been taken into account. Besides, the material characterization for the melt has also been inferred with caution. Indeed, to reproduce experimentally the genuine constitutive material of industrial foams is not an easy task as explained earlier. One simplification concerning the physics of the model is to describe the radial viscous stress and the surface tension effect of a single bubble, and then to describe the interactions between several bubbles by a linear superposition. Recently, Heitkam *et al.* [36] described the interaction of a small bubble with a wall or with another bubble. These authors showed that the hydrodynamic collision impact is the result of three contributing forces: an elastic and a viscous force along the normal direction, and a tangential viscous force. Therefore, our linear superposition of overlapping radial viscous forces might seem an oversimplification. However, it has also the advantage to indirectly generate a tangential component of the viscous flow by the counteracting forces when approaching bubbles meet. Despite its simplifications, our model opens a new route for generating microstructural topologies that resemble the real ones encountered in polymeric solid foams.

To our knowledge, such a model has not been proposed yet in the literature. Moreover, the generated microstructures can be used further as templates for investigating the mechanical behavior and relate macroscopic properties of solid foams with morphometry and local microstructure.

Thus, the mechanical properties of generated foam models were compared to spherical cells models organized as face-centred cubic (FCC), body centred cubic (BCC) or to polygonal cells (Kelvin's cell) for the same level of porosity showed significant differences. Elastic properties are rather isotropic in the realistic representation whereas they are anisotropic in case of geometrically based models. Simple geometrics consideration may explain these anisotropies. When stretching occurs, i.e. when loading axis is parallel to the strut axis [001], reinforcement is observed whereas for loading direction as [111] struts will undergo a bending load and be less relevant, explaining the weakening. This is accordance with previous studies [35] drawn up from the beam theory and that demonstrated scaling laws as $E \sim (1-\phi_v)^2$ for bending-dominated elastic behavior and $E \sim (1-\phi_v)$for stretching dominated structure. Also, values for the Young's modulus are quite different given relevance to the well-admitted idea that foam properties are not only porosity dependent. Close packing of equal spheres used to represent foam behavior seems to be not well fitted as it overestimates the properties in both elastic and plateau regimes. For the guidance of mechanical reinforcement it is rather clear that spherical voids are a good solution, especially when organized as FCC.

To accurately estimate the large strain behavior of polymer foams, the need for a near to perfect representation of the microstructure proven for low density foams [2] remains true for denser foams and even with porosity as low as 0.6, it can be hazardous to consider foam as a dense packing of perfect spheres. Behind this representation, stress localizations that may occur in real foam are hindered and this is at the base of the observed differences. Even when Kelvin's tetrakaidecahedron cell shape is chosen, shear bands cannot develop in the same ways as in realistic foam microstructures leading to some discrepancies. For sake of brevity, the mechanisms to which reference is made are not detailed here. By allowing a close to real foam representation, the "ad-hoc" modeling is able to statistically reproduce the localized deformations mainly responsible for the overall mechanical behavior as observed experimentally.

V. CONCLUSION

Statistically, the generated and real microstructures are very similar except for a few small geometrical differences in the microstructure scale. When the microstructure is observed as a whole, the generated model gives a close representation of the morphology of the real polymeric foam. Based on data values of foaming process parameters and polymer melt characteristic properties, a wide spectrum of microstructures with diverse morphologies significantly similar to those observed experimentally is obtained. Thus, our physically based model appears as an engineering guideline for studying and optimizing mechanical properties. In addition it allows microstructure and properties of bulk cellular materials to be correlated as we will report in a forthcoming article. From these aspects, our modeling constitutes an original and new 3D modeler for foam microstructure and related finite element study.

ACKNOWLEDGEMENTS

The authors wish to thank Dr A. Kraynik, who has performed much of the original work in the area of foam modeling, for offering helpful suggestions in preparing the manuscript.

Additional Information

Supplementary data related to this article can be found: Supplementary_Information.docx

Competing Interests: The authors declare that they have no competing financial interest.

APPENDIX: demonstration of equation 7

To express the stress field $\vec{\sigma}(r,t)$ in the melt, the three governing equations 4-6 described in the main text are used. They are:

$$\rho\left(\frac{\partial\vec{v}}{\partial t}+\left(\vec{v}.\vec{\nabla}\right)\vec{v}\right)=\rho\left(\frac{D^2\vec{u}}{Dt^2}\right)=\vec{\nabla}.\bar{\bar{\sigma}} \qquad \text{(eq. 1)}$$

$$\bar{\bar{\sigma}}=K_T\bar{\bar{\varepsilon}}+\eta_T\dot{\bar{\bar{\varepsilon}}} \qquad \text{(eq. 2)}$$

$$\bar{\bar{\varepsilon}}=\frac{1}{2}(\vec{\nabla}\vec{u}+\left(\vec{\nabla}\vec{u}\right)^T) \qquad \text{(eq. 3)}$$

Applying the divergence to eq.1 gives:

$$\vec{\nabla}\left[\rho\left(\frac{D^2\vec{u}}{Dt^2}\right)\right]=\Delta\boldsymbol{\sigma}$$

$$\rho_0\vec{\nabla}\left(\frac{D^2\vec{u}}{Dt^2}\right)=\frac{1}{r^2}\frac{\partial}{\partial r}\left(r^2\frac{\partial\sigma}{\partial r}\right) \qquad \text{(eq. 4)}$$

with $\rho\approx\rho_0=cte$ at first approximation. Thus:

$$\frac{D\vec{u}}{Dt}=\frac{Du}{Dt}\vec{u}_r=\frac{\partial\vec{u}}{\partial t}+v\frac{\partial\vec{u}}{\partial r}$$

$$\frac{Du}{Dt}=\frac{\partial u}{\partial t}+\frac{Du}{Dt}.\frac{\partial u}{\partial r}=\frac{\partial u}{\partial t}+\frac{\partial u}{\partial t}.\frac{\partial u}{\partial r}+o\left(\frac{\partial u}{\partial t}.\frac{\partial u}{\partial r}\right)$$

$$\frac{Du}{Dt}=\frac{\partial u}{\partial t}\left(1+\frac{\partial u}{\partial r}\right)+o\left(\frac{\partial u}{\partial t}.\frac{\partial u}{\partial r}\right) \qquad \text{(eq. 5)}$$

For small displacements of the particle, one can write:

$$\frac{\partial u}{\partial r}\ll 1$$

$$\frac{Du}{Dt}\approx\frac{\partial u}{\partial t}$$

$$\frac{D^2u}{Dt}\approx\frac{\partial^2u}{\partial t^2}+\frac{\partial u}{\partial t}.\frac{\partial^2u}{\partial r\partial t}$$

The term $\frac{\partial^2u}{\partial t^2}$ is of the order $\frac{V}{\tau}$, where V is the particle velocity whereas the term $\frac{\partial u}{\partial t}.\frac{\partial^2u}{\partial r\partial t}$ is of the order $\frac{V^2}{c\tau}$, where c is the wave velocity. By supposing small particle velocity compared to the wave velocity:

$$V\ll c\rightarrow\frac{V^2}{c\tau}\ll\frac{V}{\tau} \qquad \text{(eq. 6)}$$

We thus approximate:

$$\frac{D^2u}{Dt^2} \approx \frac{\partial^2 u}{\partial t^2} \qquad \text{(eq. 7)}$$

Equation 4 then becomes:

$$\rho_0 \vec{\nabla}\left(\frac{D^2\vec{u}}{Dt^2}\right) = \frac{\rho_0}{r^2}\frac{\partial}{\partial r}\left(r^2\frac{\partial^2 u}{\partial t^2}\right) = \frac{1}{r^2}\frac{\partial}{\partial r}\left(r^2\frac{\partial \sigma}{\partial r}\right) \qquad \text{(eq. 8)}$$

Equation 3 express deformations tensor related to displacement:

$$\varepsilon = \frac{1}{r^2}\frac{\partial}{\partial r}(r^2 u)$$

$$\frac{\partial \varepsilon}{\partial t} = \frac{1}{r^2}\frac{\partial}{\partial r}\left(r^2\frac{\partial u}{\partial t}\right)$$

$$\frac{\partial^2 \varepsilon}{\partial t^2} = \frac{1}{r^2}\frac{\partial}{\partial r}\left(r^2\frac{\partial^2 u}{\partial t^2}\right) \qquad \text{(eq. 9)}$$

This applied to equation 8 gives:

$$\rho_0\left(\frac{\partial^2 \varepsilon}{\partial t^2}\right) = \frac{1}{r^2}\frac{\partial}{\partial r}\left(r^2\frac{\partial \sigma}{\partial r}\right) \qquad \text{(eq. 10)}$$

With the variables changes $\sigma' = r\sigma$ and $\varepsilon' = r\varepsilon$:

$$\frac{1}{r^2}\frac{\partial}{\partial r}\left(r^2\frac{\partial \sigma}{\partial r}\right) = \frac{2}{r}\frac{\partial \sigma}{\partial r} + \frac{\partial^2 \sigma}{\partial r^2} = \frac{1}{r}\frac{\partial^2 \sigma'}{\partial r^2}$$

$$\rho_0 r\left(\frac{\partial^2 \varepsilon}{\partial t^2}\right) = \frac{\partial^2 \sigma'}{\partial r^2}$$

$$\rho_0\left(\frac{\partial^2 \varepsilon'}{\partial t^2}\right) = \frac{\partial^2 \sigma'}{\partial r^2} \qquad \text{(eq. 11)}$$

And (eq. 2):

$$\sigma' = K_T \varepsilon' + \eta_T \frac{\partial \varepsilon'}{\partial t} \qquad \text{(eq. 12)}$$

In order to obtain one unique final equation as a function of the stress field, eq. 12 is derived regarding the time *t*. In this equation, the viscosity, η_{T}, and the elastic modulus, E_T, depend on temperature and thus on time:

$$\eta_{\mathrm{T}} = \eta_0 \exp\left[\frac{\mathrm{E_A}}{\mathrm{R}}\left(\frac{1}{\mathrm{T}} - \frac{1}{\mathrm{T_0}}\right)\right]$$

$$K_T = \frac{1}{3}\frac{E_T}{1-2v}$$

$$E_T = E_0 \exp[a(T_0 - T)]$$

$$T(t) = T_0 - \frac{(T_0 - T_1)}{t_1} t$$

where T_0 is the initial temperature before the foam expansion.

The terms $\frac{E_A}{R}$ and the constant a are determined by the initial and final conditions on viscoelasticity:

$$\frac{E_A}{R} = \frac{log\frac{\eta_1}{\eta_0}}{\left(\frac{1}{T_1} - \frac{1}{T_0}\right)}$$

$$a = -\frac{log\frac{E_1}{E_0}}{(T_1 - T_0)}$$

η_0, E_0, T_0, η_1 , E_1 and T_1 are viscosity, elastic modulus and temperature of the melt at the beginning and at the end of the process, respectively.

By derivative of eq. 12 regarding time, it gives:

- First order derivation:

$$\frac{\partial \sigma'}{\partial t} = \frac{dK_T}{dt}\varepsilon' + K_T\frac{\partial \varepsilon'}{\partial t} + \frac{d\eta_T}{dt}\frac{\partial \varepsilon'}{\partial t} + \eta_T\frac{\partial^2 \varepsilon'}{\partial t^2}$$

note that the time derivatives of K_T and η_T are full derivatives rather than partial derivatives since the temperature field is spatially uniform in the whole mixture.

- Second derivation:

$$\frac{\partial^2 \sigma'}{\partial t^2} = \frac{d^2K_T}{dt^2}\varepsilon' + \left[2\frac{dK_T}{dt} + \frac{d^2\eta_T}{dt^2}\right]\frac{\partial \varepsilon'}{\partial t} + \left[K_T + 2\frac{d\eta_T}{dt}\right]\frac{\partial^2 \varepsilon'}{\partial t^2} + \eta_T\frac{\partial^3 \varepsilon'}{\partial t^3}$$

With, $\frac{dK_T}{dt} = \frac{dK_T}{dT}\frac{dT}{dt} = a\frac{(T_0 - T_1)}{t_1}K_T$

$$\frac{d^2E_T}{dt^2} = \left[a\frac{(T_0 - T_1)}{t_1}\right]^2 K_T$$

$$\frac{d\eta_T}{dt} = \frac{d\eta_T}{dT}\frac{dT}{dt} = \frac{E_A}{R}\frac{1}{T^2}\frac{(T_0 - T_1)}{t_1}\eta_T$$

$$\frac{d^2\eta_T}{dt^2} = \left[\frac{E_A}{R}\frac{1}{T^2}\frac{(T_0-T_1)}{t_1}\right]^2 \eta_T$$

It comes, the equation (eq. 13):

$$\frac{\partial^2\sigma'}{\partial t^2} = \left[a\frac{(T_0-T_1)}{t_1}\right]^2 K_T\varepsilon' + \left[2a\frac{(T_0-T_1)}{t_1}K_T + \left[\frac{E_A}{R}\frac{1}{T^2}\frac{(T_0-T_1)}{t_1}\right]^2 \eta_T\right]\frac{\partial\varepsilon'}{\partial t} + \left[K_T + 2\frac{E_A}{R}\frac{1}{T^2}\frac{(T_0-T_1)}{t_1}\eta_T\right]\frac{\partial^2\varepsilon'}{\partial t^2} + \eta_T\frac{\partial^3\varepsilon'}{\partial t^3}$$

Approximations:

In order to reduce the number of terms, we expressed their order of magnitude. The two last terms are the most dominant ones. Thus:

$$\frac{\partial^2\sigma'}{\partial t^2} = \left[K_T + 2\frac{E_A}{R}\frac{1}{T^2}\frac{(T_0-T_1)}{t_1}\eta_T\right]\frac{\partial^2\varepsilon'}{\partial t^2} + \eta_T\frac{\partial^3\varepsilon'}{\partial t^3}$$

Moreover $K_T \gg 2\frac{E_A}{R}\frac{1}{T^2}\frac{(T_0-T_1)}{t_1}\eta_T$; so:

$$\frac{\partial^2\sigma'}{\partial t^2} = K_T\frac{\partial^2\varepsilon'}{\partial t^2} + \eta_T\frac{\partial^3\varepsilon'}{\partial t^3} \qquad \text{(eq. 14)}$$

The term $K_T\frac{\partial^2\varepsilon'}{\partial t^2}$ expresses the influence of the elastic component of the melt on the flow and the term $\eta_T\frac{\partial^3\varepsilon'}{\partial t^3}$ the one for the viscosity.

By using equation (eq. 11) we finally obtain:

$$\frac{\partial^2\sigma'}{\partial t^2} = \frac{1}{\rho_0}K_T\frac{\partial^2\sigma'}{\partial r^2} + \frac{\eta_T}{\rho_0}\frac{\partial^3\sigma'}{\partial t\partial r^2}$$

$$\frac{\partial^2\sigma'}{\partial r^2} - \frac{1}{c^2}\frac{\partial^2\sigma'}{\partial t^2} + \frac{\eta_T}{K_T}\frac{\partial^3\sigma'}{\partial t\partial r^2} = 0 \text{ with, } c = \sqrt{\frac{K_T}{\rho_0}} \qquad \text{(eq. 15)}$$

References

[1] W. Thomson (Lord Kelvin), "*On the Division of Space with Minimum Partitional Area*", Phil. Mag. 24, 503 (1887).

[2] W. E. Warren and A. M. Kraynik, "*Linear elastic behavior of a low-density Kelvin foam with open cells*", J. Appl. Mech. 64, 787 (1997).

[3] E. B. Matzke, "*The three-dimensional shape of bubbles in foam-an analysis of the role of surface forces in three-dimensional cell shape determination*", American Journal of Botany 58-80 (1946).

[4] P. Roberts and E. J. Garboczi, "*Elastic moduli of model random three-dimensional closed-cell cellular solids*", Acta Mater. 49, 189 (2001).

[5] V. P. Valuyskikh, "*Computer simulation of structure and calculation of physico-mechanical characteristics and foamed plastics*", Cell. Polym. 9, 109 (1990).

[6] A. M. Kraynik, "*The Structure of Random Foam*", Adv. Eng. Mater. 9, 900 (2006).

[7] K.A. Brakke, *The surface evolver*, Experimental Mathematics 1, 141 (1992)

[8] J.L. Grenestedt , "*Influence of Wavy Imperfections in Cell Walls on Elastic Stiffness of Cellular Solids*", J. Mech. Phys. Solids (1998) 46 (1) 29–50.

[9] Grenestedt, J.L., Tanaka, K., Influence of cell shape variations on elastic stiffness of closed cell cellular solids. *Scr. Mater.* (1999) 40 71–77.

[10] Grenestedt, J.L., Bassinet, F., Influence of cell wall thickness variations on elastic stiffness of closed cell cellular solids. *Int. J. Mech. Sci.* (2000) 42 1327–1338.

[11] D. Langevin and M. Vignes-Adler, "*Microgravity studies of aqueous wet foams*", Eur. Phys. J. E 37, 16 (2014).

[12] M. Dabo, "*Analyse du comportement mécanique des mousses polymères : apport de la tomographie X et de la simulation numérique*", Ph. D thesis, Université de Strasbourg (2015)

[13] J. Elliott, H. Windle, J. R. Hobdell, G. Eeckhaut, R. J. Oldman, W. Ludwig, E. Boller, P. Cloetens, and J. Baruchel, "*In-situ deformation of an open-cell flexible polyurethane foam characterised by 3D computed microtomography*", J. Mater. Sci. 37, 1547 (2002).

[14] M. D. Montminy, A. R. Tannenbaum, and C. W. MacOsko, "*The 3D structure of real polymer foams,"* J. Colloid Interf. Sci. 280, 202 (2004).

[15] S. Youssef, E. Maire, and R. Gaertner, *"Finite element modelling of the actual structure of cellular materials determined by X-ray tomography",* Acta Materialia, vol. 53, pp. 719-730, 2005.

[16] P. Kékicheff, M. Dabo, G. Dalongeville, C. Gauthier, and T. Roland, "*Polymeric solid foams: microstructure, topology and defects determined by high resolution X-ray microtomography*", Macromol. Symp. 369, 56 (2016).

[17] M-C. Heuzey, "*Fluides viscoélastiques : modélisation numérique et mesures expérimentales*", Ph. D. Thesis, Université Mc Gill, Montréal, Canada (1999).

[18] A. D. Drozdov, "*Viscoelastoplasticity of amorphous glassy polymers"*, Eur. Polym. J. 36, 2063 (2000).

[19] G. C. Berry and T. G. Fox, "*The viscosity of polymers and their concentrated solutions*", Adv. Polym. Sci. 5, 261 (1968).

[20] M. L. Williams, R. F. Landel, and J. D. Ferry, "*The Temperature Dependence of Relaxation Mechanisms in Amorphous Polymers and Other Glassforming Liquids*", Amer. Chem. Soc77, 3701 (1955).

[21] N.D. Hari Dass, "*The Principles of Thermodynamics*", CRC Press, Taylor and Francis Group, ISBN 13:978-1-4665-1208-5.

[22] R. Temam, *Navier-Stokes equations: theory and numerical analysis*, American Mathematical Soc., vol. 343, ISBN 978-0-8218-2737-6 (1984).

[23] H. Schiessel, R. Metzler, A. Blumen, and T. F. Nonnenmacher, "*Generalized viscoelastic models: their fractional equations with solutions*", J. Phys. A. Math. Gen. 28, 6567 (1995).

[24] J. G. Heywood and R. Rannacher, "*Finite element approximation of the nonstationary Navier-Stokes problem. I. Regularity of solutions and second-order error estimates for spatial discretization*", SIAM J. Numer. Anal. 19, 275 (1982).

[25] J. Topper and T. Kawahara, "*Approximate equations for long nonlinear waves on a viscous fluid*", J. Phys. Soc. Japan 44, 663 (1978).

[26] A. Bedford and D. S. Drumheller, "*Introduction to Elastic Wave Propagation*", J. Wiley 297, ISBN 0-471-93884-X (1994).

[27] A. W. Adamson, A. P. Gast, and others, "*Physical chemistry of surfaces*" ISBN: 978-0-471-14873-9 (1997).

[28] J. J. Feng and C. a. Bertelo, "*Prediction of bubble growth and size distribution in polymer foaming based on a new heterogeneous nucleation model*", J. Rheol. 48, 439 (2004).

[29] I. Khan, S. Costeux, D. Adrian, and S. Bunker, "*Numerical Studies of Nucleation and Bubble Growth in Thermoplastic Foams at high Nucleation Rates*", FOAMS conference proceedings; SPE: Seattle, WA, (2013).

[30] M. Torrecilla, "*Introduction to numerical simulation of fluid flows*" JASS 04, St Petersburg (2004).

[31] Jang W., Kyriakides S., Kraynik A., "*On the compressive strength of open-cell metal foams with Kelvin and random cell structures*", Int. J. Solids Struct. 47, 2872 (2010).

[32] M. Yu, P. Zhu, Y. Ma, "*Effects of particle clustering on the tensile properties and failure mechanisms of hollow spheres filled syntactic foams: A numerical investigation by microstructure based modeling*", Materials and Design 47, 80 (2013).

[33] R. M. Christensen, "*Mechanics of low density materials*", J. Mech. Phy. Solids 34, 563 (1990).

[34] Heitkam, S., Drenckhan, W., Titscher, T., Kreuter, D., Hajnal, D., Piechon, F., Fröhlich, J.: "*Elastic Properties of Material with Spherical Voids in Different Arrangements*", Eur. J. Mech. A/Solids 59, 252 (2016).

[35] Gibson, L.J., Ashby, M.F.: Cellular Solids: Structure and Properties, 2nd edn. Cambridge University Press, Cambridge (1997).

[36] S. Heitkam, AE Sommer , W Drenckhan, J.A. Fröhlich, "*Simple collision model for small bubbles*", J Phys Condens Matter. 29, (12) (2017)

Figure captions

Figure 1: SEM observations of industrial elastomeric closed-cell foam microstructures of respectively (a) 58% and (b) 82% porosity. The cells shapes are neither circular nor polygonal and several imperfections inherent to the industrial process are present (holes in the cell wall).

Figure 2: Illustration of the two concepts on which the model for interacting cells is based. Every cell (contour drawn in red) creates an influence zone in the melt (grey) surrounding it. As a result the nucleation of new additional cells (in blue) may occur only away from this restricted zone. As time elapses, the already nucleated cells grow and expand in the melt and the potential nucleation zone (in black) shrinks

Figure 3: 2D microstructures generated for different time distribution profiles for the cells nucleation. In these simulations all other parameters were kept constant (screening length δ = 90 µm; surface tension γ_0 = 15 mN/m). Note the overall porosity is used as convergence criteria, here $P = 85 \pm 1$ %. Quasi-monodispersity is observed only when the cells nucleate simultaneously (type 1 distribution; left) and $C_{vol} = 0.14$. Otherwise $C_{vol} = 1.63 > 1$ when cells nucleate with delay (type 2 distribution; middle) with two marked populations of cell sizes; and $C_{vol} = 0.44$ when the nucleation follows a Gaussian temporal law (right). Note the different expansion scales for the growing cells.

Figure 4: Influence of an increasing screening length, δ, on the 2D microstructures generated when all cells nucleate simultaneously (type 1 distribution of Fig. 3), all other parameters being kept constant. The obtained porosity, P, decreases and the polydispersity in cell sizes, C_{vol}, slightly increases but still remains small. *Left*: δ = 56 µm, P = 90%, C_{vol} = 0.08; *middle*: δ = 76 µm, P = 85%, C_{vol} = 0.12; *right*: δ = 133 µm, P = 72%, C_{vol} = 0.16. Note that an event of two encountering cells leads to their coalescence as illustrated by the arrow.

Figure 5: Influence of an increasing surface tension, γ, on the 2D microstructures generated when all cells nucleate simultaneously (type 1 distribution of Fig. 2), all other parameters being kept constant (screening length δ = 70 µm). The obtained porosity, P, decreases and the polydispersity in cell sizes, C_{vol}, increases. *Left*: $\gamma = \gamma_0$, P = 86%, C_{vol} = 0.10; *middle* : γ = 1.6 γ_0, P = 85%, C_{vol} = 0.16; *right*: γ = 2.0 γ_0, P = 47%, C_{vol} = 0.29.

Figure 6: Reconstruction of a 3D microstructure. After having obtained the cellular structure by numerical simulation (a), the contour surfaces of the cells are created (b) from which the microstructure is extracted (c); see main text. Different porosities and polydispersities can thus be generated: (d) $P = 59\%$, $C_{vol} = 0.35$; (e) $P = 73\%$, $C_{vol} = 0.33$; (f) $P = 75\%$, $C_{vol} = 1.37$.

Figure 7: Sketch of the numerical models, from left to right: a) Body-centred cubic (BCC), b) Face-centred cubic (FCC), c) Kelvin's tetrakaidecahedron structure d) "ad-hoc" model.

Figure 8: Large strain compressive behavior of foams – comparisons between numerical models and experiments

Figure 9: Comparison between a microstructure generated by numerical simulation (left, $P = 58.5\%$) and a polymeric closed-cell foam measured by X-ray microtomography at high spatial resolution (right, $P = 56.0\%$). Height/diameter is of 1.2 mm. *Top*: 3D reconstruction. *Bottom*: Two longitudinal sections emphasizing the close agreement between the respective spatial distributions of the cells in terms of their position, shape, and orientation, despite a few discrepancies outlined by the arrows.

Figure 10: Sphericity and equivalent diameter distributions for the cells of the microstructures generated by numerical simulation (black) and compared to real polymeric closed-cell foams (red) of same porosity (cf. Fig.9).

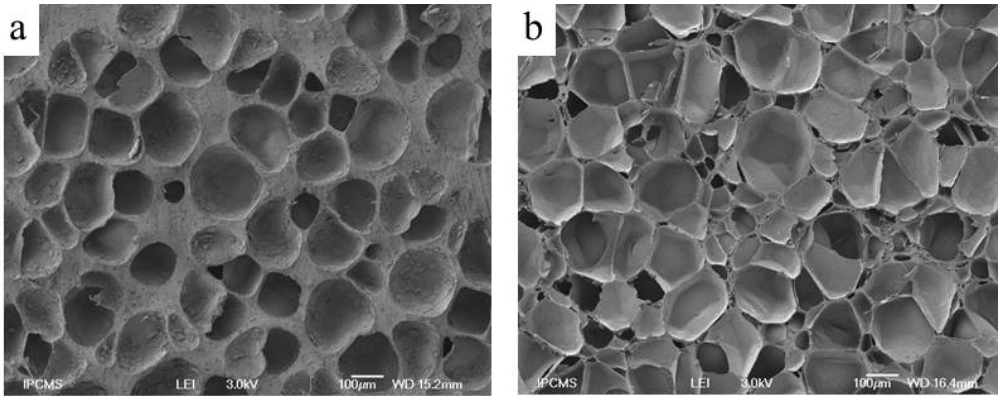
a
b
IPCMS
LEI
3.0kV
100µm
WD 15.2mm
IPCMS
LEI
3.0kV
100µm
WD 16.4mm

Figure 1

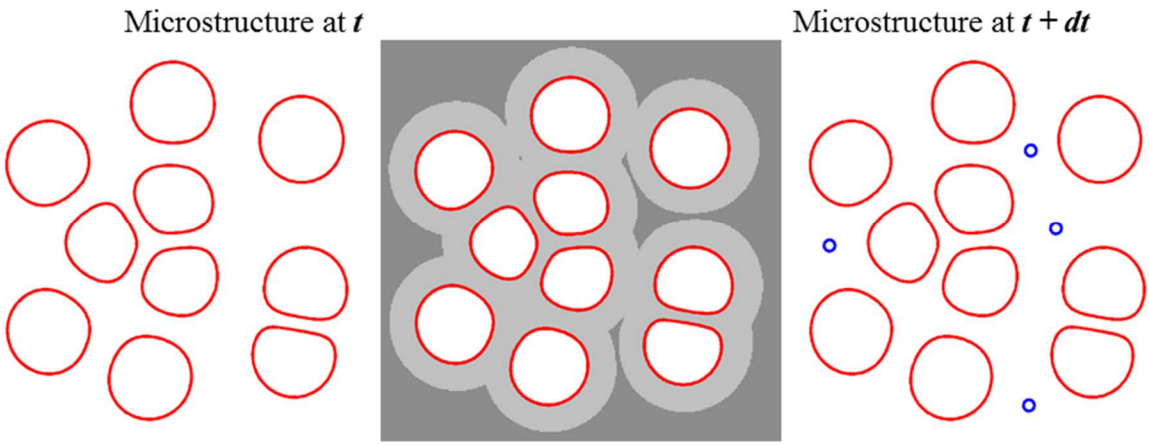

Figure 2

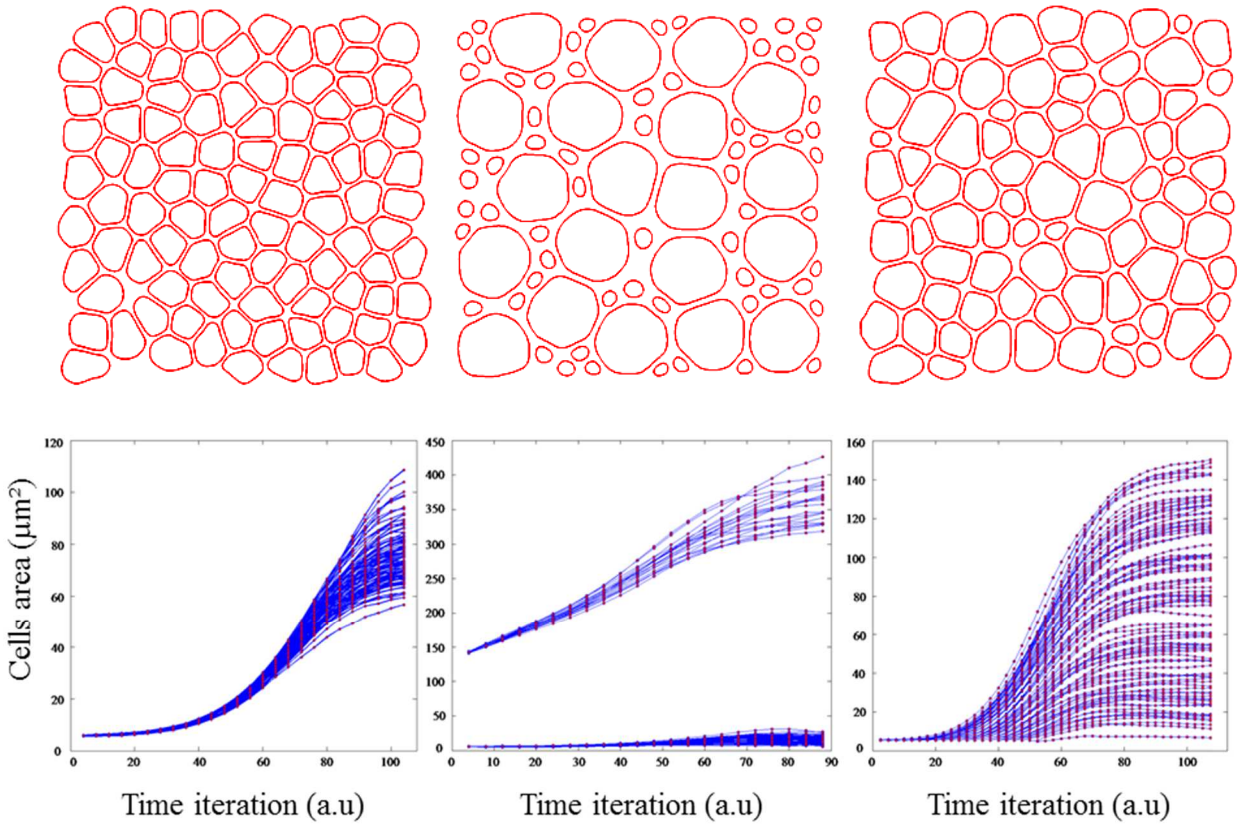
Cells area (µm²)
Time iteration (a.u)
Time iteration (a.u)
Time iteration (a.u)

Figure 3

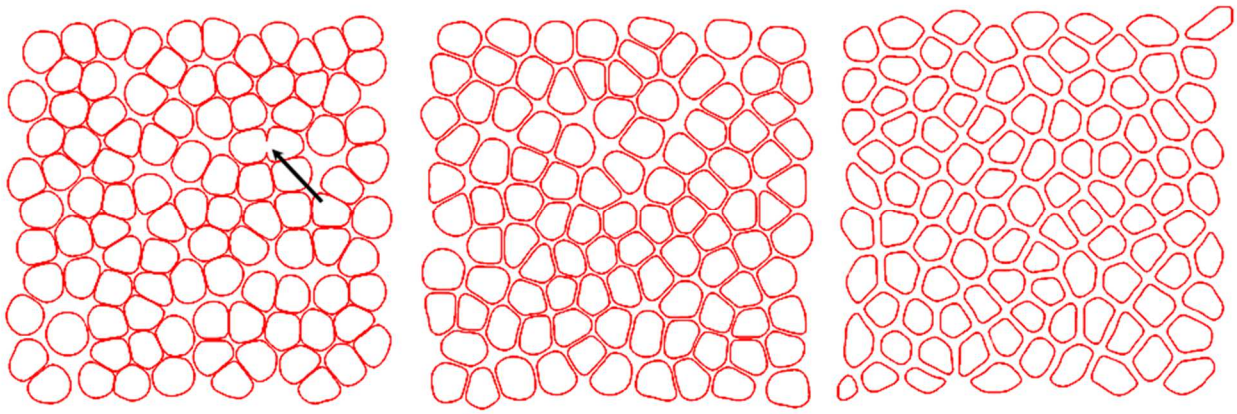

Figure 4

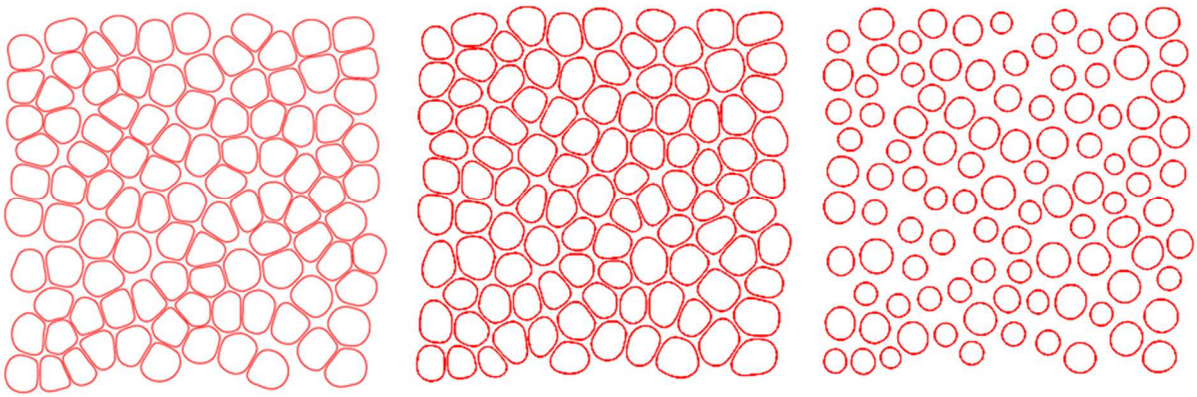

Figure 5

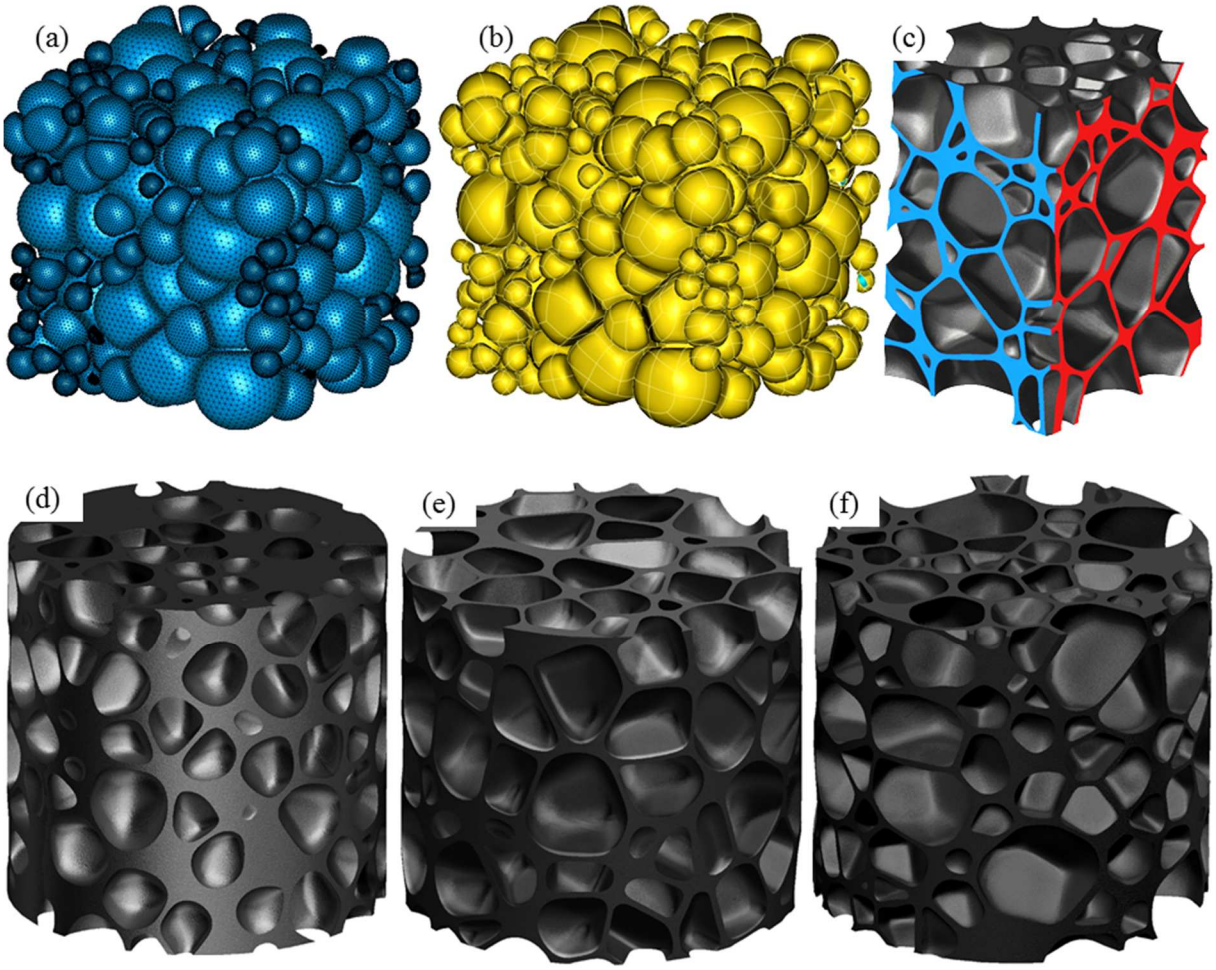

Figure 6

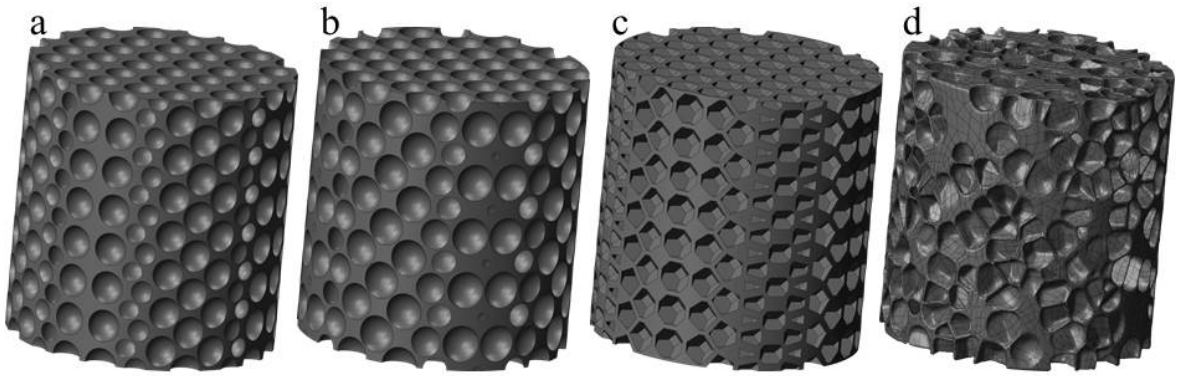

Figure 7

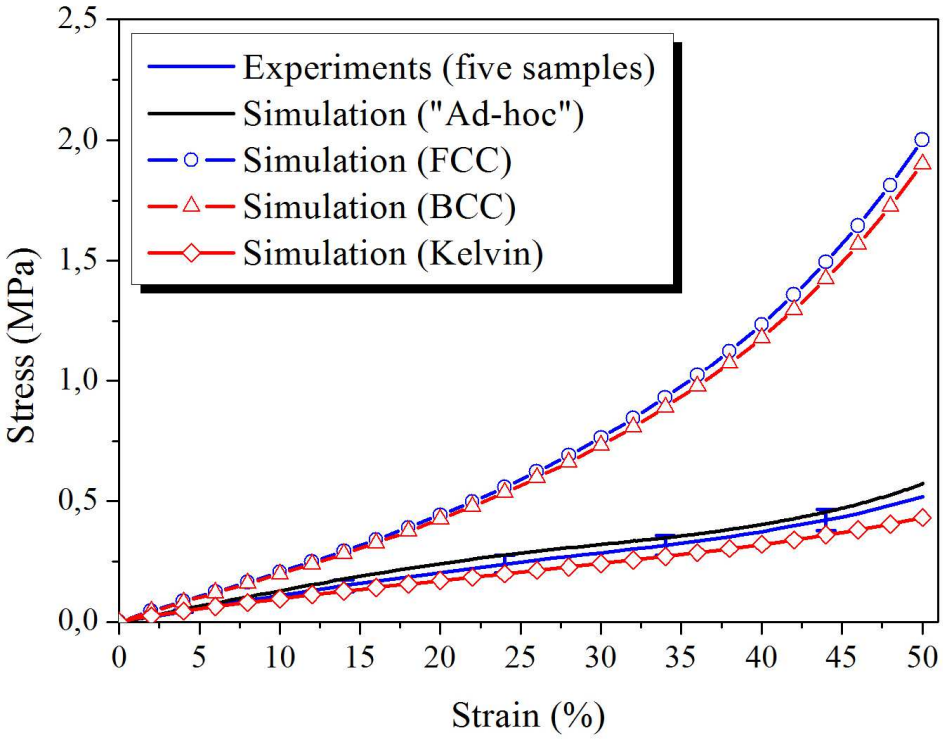
Experiments (five samples)
Simulation ("Ad-hoc")
Simulation (FCC)
Simulation (BCC)
Simulation (Kelvin)
Stress (MPa)
Strain (%)
0,0
0,5
1,0
1,5
2,0
2,5
0
5
10
15
20
25
30
35
40
45
50

Figure 8

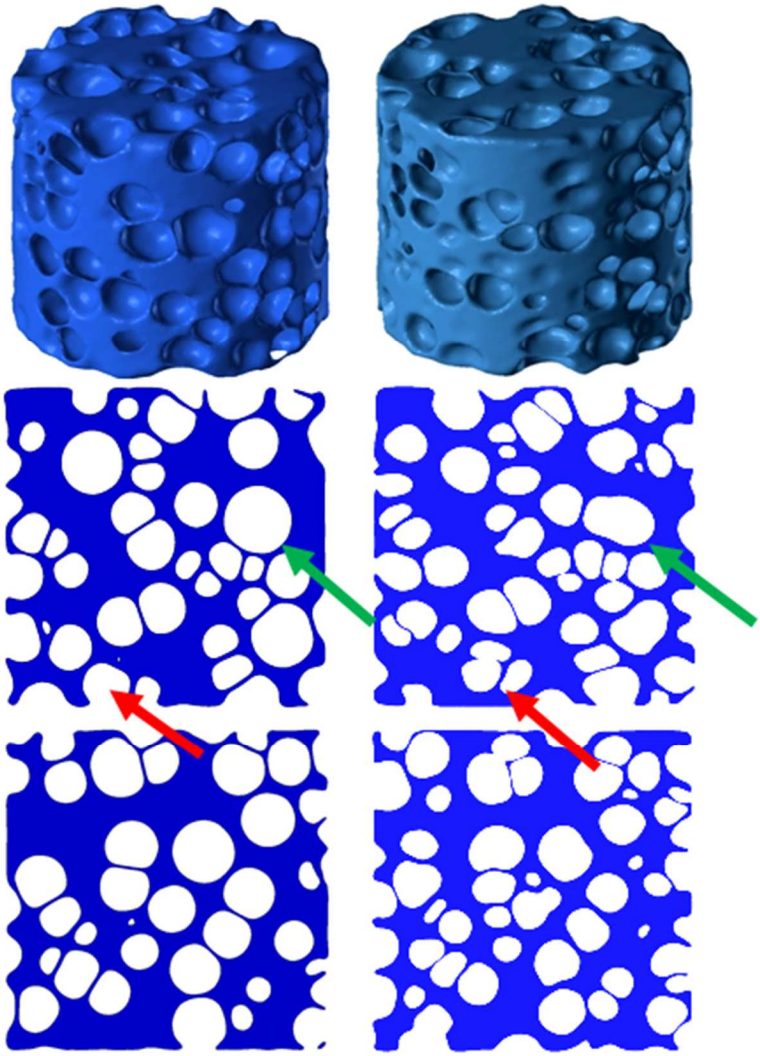

Figure 9

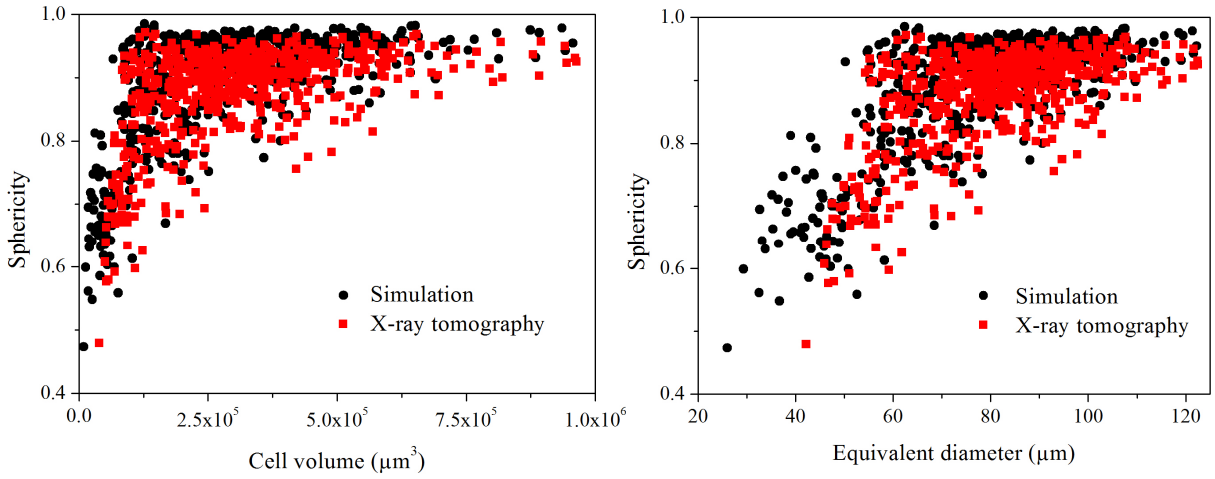
1.0
0.8
0.6
0.4
Sphericity
0.0
2.5x10^5
5.0x10^5
7.5x10^5
1.0x10^6
Cell volume (μm^3)
Simulation
X-ray tomography
1.0
0.8
0.6
0.4
Sphericity
20
40
60
80
100
120
Equivalent diameter (μm)
Simulation
X-ray tomography

Figure 10